

Influence of Natural Climate Variability on Extreme Wave Power over Indo-Pacific Ocean Assessed using ERA5

Prashant Kumar (✉ prashantkumar@nitdelhi.ac.in)

National Institute of Technology, Delhi <https://orcid.org/0000-0001-8480-7490>

Sukhwinder Kaur

National Institute of Technology Delhi

Evan Weller

University of Auckland

Ian R. Young

University of Melbourne

Research Article

Keywords: Wave power energy, Climate Variability, Generalized extreme value(GEV)distribution, Indo-Pacific Ocean

Posted Date: April 7th, 2021

DOI: <https://doi.org/10.21203/rs.3.rs-372607/v1>

License:   This work is licensed under a Creative Commons Attribution 4.0 International License.

[Read Full License](#)

Version of Record: A version of this preprint was published at Climate Dynamics on October 4th, 2021. See the published version at <https://doi.org/10.1007/s00382-021-05981-9>.

1 **Influence of Natural Climate Variability on Extreme Wave Power over Indo-Pacific Ocean**
2 **Assessed using ERA5**

3 Sukhwinder Kaur¹, Prashant Kumar¹, Evan Weller², Ian R. Young³

4 ¹Department of Applied Sciences, National Institute of Technology Delhi, Delhi, India

5 ²School of Environment, University of Auckland, Auckland, New Zealand

6 ³Department of Infrastructure Engineering, University of Melbourne, Australia.

7

8

9

10 Version: 09-03-2021

11

12

13

14

15

16

17

18

19

20

21

22 *Corresponding Author

23 Email: prashantkumar@nitdelhi.ac.in

24

25

27 In recent decades, wave power (WP) energy from the ocean is one of the cleanest renewable
28 energy sources associated with oceanic warming. In Indo-Pacific Ocean, the WP is significantly
29 influenced by natural climate variabilities, such as El Niño Southern Oscillation (ENSO), Indian
30 Ocean Dipole (IOD) and Pacific Decadal Oscillation (PDO). In this study, the impact of major
31 climate variability modes on seasonal extreme WP is examined over the period 1979–2019 using
32 ERA5 reanalysis data and the non-stationary generalized extreme value analysis is applied to
33 estimate the climatic extremes. Independent ENSO influence after removing the IOD trends
34 ($ENSO|_{IOD}$) on WP are evident over the eastern and central Pacific during December–February
35 (DJF) and March–May (MAM), respectively, which subsequently shifts towards the western
36 Pacific in June–August (JJA) and September–November (SON). The $ENSO|_{PDO}$ impact on WP
37 exhibits similar yet weaker intensity year round compared to ENSO. Extreme WP responses due
38 to the $IOD|_{ENSO}$ include widespread decreases over the tropical and eastern Indian Ocean (IO),
39 with localized increases only over the South China and Philippine (SCP) seas and Bay of Bengal
40 (BOB) during JJA, and the Arabian Sea during SON. Lastly, for the $PDO|_{ENSO}$, the significant
41 increases in WP are mostly confined to the Pacific, and most prominent in the North Pacific.
42 Composite analysis of different phase combinations of PDO (IOD) with El Niño (La Niña)
43 reveals stronger (weaker) influences year-round. The response patterns in significant wave height
44 (SWH), peak wave period (PWP), sea surface temperatures (SST), and sea level pressure (SLP)
45 helps to explain the seasonal variations in WP.

46

47 **Keywords:** Wave power energy, Climate Variability, Generalized extreme
48 value(GEV)distribution, Indo-Pacific Ocean,

49

50 **1. Introduction**

51 The depletion of conventional energy resources and increasing global warming due to the
52 consumption of fossil fuels have prompted interest in renewable energy resources in many
53 countries (Cornett 2008). Among the various renewable energy resources such as wind, solar,
54 hydro-power, etc., wave power is one of the most important and least studied renewable energy
55 resources. Recent studies suggest that the spatial and temporal variations in wave power are
56 induced by natural climate variabilities like El Niño–Southern Oscillation (ENSO), Pacific
57 Decadal Oscillation (PDO), and Atlantic Multidecadal Oscillation (AMO) (Bromirski and Cayan
58 2015; Bromirski et al. 2013; Reguero et al. 2019; Yang and Oh 2020). Therefore, a better
59 comprehension of the wave power and its relation with natural climate variability is essential for
60 social and economic development.

61 WP, which measures the transport of energy that is transmitted by air-to-sea exchanges and used
62 for wave motion (Donelan et al. 1997; Reguero et al. 2019), depends not only on wave height but
63 also on wave period. Moreover, WP represents the accumulated wave energy over periods of
64 time such as months, seasons, and years, unlike other wave climate parameters (e.g., SWH) that
65 must be averaged (Reguero et al. 2019). Therefore, WP can represent the variations in the wave
66 climate better than other wave parameters (e.g., wave height). Yet, to date, continuous efforts
67 have been made to analyze the mean and extreme historical trends in wind and wave climate at
68 the global (Aarnes et al. 2015; Caires et al. 2006; Fan et al. 2012; Gulev and Grigorieva 2004;
69 Meucci et al. 2020; Reguero et al. 2012; Stopa et al. 2013; Young et al. 2011, 2012; Young and
70 Ribal 2019) and regional scale (Allan and Komar 2006; Carter and Draper 1988; Gulev and
71 Grigorieva 2006; Hemer et al. 2008, 2010; Menendez et al. 2008; Wang and Swail 2001, 2006;
72 Wang et al. 2009, 20012; Young 1999; Young and Ribal 2019). In addition, other wave climate

73 indicators, such as wave period and/or direction, have also been investigated extensively to
74 identify underlying properties in the changes to mean and extreme SWH (Chen et al. 2002;
75 Semedo et al. 2011; Sterl and Caires 2005; Young 1999; Zhang et al. 2011; Zheng et al. 2016).

76 In context of WP, several studies have been carried out previously to analyze the monthly and
77 annual variations in mean wave power at the global scale (Arinaga and Cheung 2012; Barstow et
78 al. 2008; Cornett 2008; Gunn and Stock-Williams 2012; Hulls 1977; Mollison 1986; Mork et al.
79 2010). Further, the seasonal variations in mean wave power were examined by Mackay (2012).
80 However, these analyses were conducted based on either satellite data or wave models such as
81 Wave Watch-III (WW3) and ECMWF WAM for relatively short periods of 6 or 10 or 12 years.
82 Long term seasonal and interannual variations in global mean wave power were investigated by
83 Reguero et al (2015) using WW3 data for a 61-year period (1948–2008). In this regard,
84 numerous regional studies have also been conducted. For example, the North Pacific (NP)
85 (Bromirski et al. 2005, 2013; Yang and Oh 2020), North Atlantic (NA) (Bromirski and Kossin
86 2008; Bromirski and Cayan 2015; Santo et al. 2015), Black Sea (Aydogan et al. 2013), along the
87 Australian coasts (Hemer et al. 2016, 2018), and shelf seas of India (Kumar and Anoop 2015;
88 Sannasiraj and Sundar, 2016; Amrutha et al. 2019; Amrutha and Kumar 2020). However,
89 seasonal/annual variations in extreme WP have not been assessed yet at the global and regional
90 scale.

91 Although many studies have focused on seasonal/annual variations in mean WP as described
92 above, the natural climate variabilities such as the El Niño–Southern Oscillation (ENSO), Indian
93 Ocean Dipole (IOD), and Pacific Decadal Oscillation (PDO), etc. can exert a significant impact
94 on wave climate through large-scale atmospheric circulation patterns with different seasonal and
95 regional features (Hemer et al. 2010; Izaguirre et al. 2010, 2011; Kumar et al 2016, 2019;

96 Marshall et al. 2018; Menéndez et al. 2008; Patra et al. 2020; Wandres et al. 2018; Yang and Oh
97 2018). However, influences due to such large-scale natural climate variability modes on WP
98 remains unclear, except for limited regional and global scale studies. For example, using the
99 WW3 wave model for the period 1948-2008, the PDO influence on WP across the NP region
100 was investigated by Bromirski et al. (2013) and NAO influence on WP across the NA region by
101 Bromirski and Cayan (2015) during winter (November–March) and summer (May–September).
102 Recently, Yang and Oh (2020) examined the effect of ENSO and PDO on WP during boreal
103 summer (June-August, JJA) in the western NP. At the global scale, Reguero et al. (2015)
104 analyzed the interrelation between the annual mean WP and fifteen climate variability modes
105 which include ENSO, IOD, and PDO. Recently, the ENSO and Atlantic Multidecadal Oscillation
106 (AMO) influence on annual mean WP have been reported by Reguero et al. (2019). Such studies
107 were predominantly concerned with the seasonal/annual impact of natural climate variability on
108 mean WP.

109 “Extreme” events are significant departures from the normal climate state and often have
110 widespread societal and ecological impacts. The changes in extreme and mean wave
111 characteristics have been reported to be of different nature (Feng et al. 2012; Mori et al. 2010),
112 and are observed to be linked with more frequent extreme events. So, it’s crucial to analyze the
113 influence of natural climate variability on extreme parameters, which exert stronger impacts than
114 mean. Further, the simple linear regression analysis is used for mean variables and cannot be
115 applied to extreme variables because of their non-normality nature (Coles 2001), and recent
116 studies have widely used the extreme value theory to investigate the impact of climate variability
117 on extreme parameters such as SWH, wind, wave period, etc. (Izaguirre et al. 2010, 2011;
118 Kharin and Zwiers 2005; Kumar et al 2016, 2019; Menéndez et al. 2008; Min et al. 2013; Patra

119 et al. 2020; Zhang et al. 2010). But still, none of the previous studies assessed the impact of
120 natural climate variability on extreme WP.

121 This study investigates the seasonal influence of dominant modes of natural climate variability,
122 such as ENSO, IOD, and PDO on extreme WP in the Indo–Pacific Ocean using ERA5 reanalysis
123 data for the 41 year period from 1979–2019. For this purpose, firstly, the four boreal seasons
124 (i.e., December–February (DJF, winter), March–May (MAM, spring), June–August (JJA,
125 summer), and September–November (SON, autumn)) are considered to understand the seasonal
126 influence of natural climate variability on extreme WP and a non–stationary generalized extreme
127 value GEV analysis (Kharin and Zwiers 2005; Zhang et al. 2010; Min et al. 2013) is applied to
128 determine/capture the seasonal extremes. Regions with statistically significant responses at the
129 5% level are marked by hatching. In addition, the seasonal influence of natural climate
130 variability on extreme SWH and Peak Wave Period (PWP) is also investigated to explore the
131 associated underlying mechanisms in enhancing or reducing the WP in the Indo-Pacific Ocean as
132 WP comprises information about SWH and PWP. The seasonal teleconnection patterns of WP
133 and SWH are explained through/by SLP and SST.

134 As different modes of natural climate variability tend to interact with each other in specific
135 seasons (Cai et al. 2011; Kumar et al. 2016, 2019). Therefore, independent analysis of seasonal
136 mean and extreme WP, SWH, and PWP is carried out to assess the role of one variability mode
137 in strengthening and weakening the other variability mode influence in different seasons.
138 Additionally, the composite analysis of mean and extreme WP for the different phase
139 combinations of natural climate variabilities (i.e. ENSO, IOD, and PDO) is also conducted to get
140 further insight into the inter-relation between different variability modes. The novelty of the
141 current study in comparison to previous relevant studies is detailed in Table 1.

142 The remainder of the paper is structured as follows. Data and methodology are detailed in section
143 2 and teleconnection patterns in section 3. Section 4 provides the detailed investigation of the
144 influence of natural climate modes (in particular the ENSO, IOD, and PDO) and their independent
145 impact on seasonal mean and extreme WP, SWH, and PWP. Composite analysis for different
146 phase combinations of ENSO with IOD and ENSO with PDO is presented in section 5. Section 6
147 provides a summary and conclusions.

148 **2. Data and Methodology**

149 **2.1. Data**

150 The latest reanalysis product from the European Centre for Medium-Range Weather Forecasting
151 (ECMWF), referred to as the ERA5 reanalysis (Hersbach and Dee 2016), is used in the present
152 study to analyze the mean and extreme WP for the 41-year period from 1979 to 2019 over the
153 Indo-Pacific region for the four boreal seasons (i.e., December–February (DJF, winter), March–
154 May (MAM, spring), June–August (JJA, summer), and September–November (SON, autumn).
155 The ERA5 reanalysis data have several advancements compared to its predecessor, ERA-Interim
156 (Dee et al. 2011). In contrast to ERA-Interim, ERA5 has higher spatial and temporal resolution
157 along with an improved representation of the tropospheric processes, including better
158 representation of tropical cyclones, global balance of precipitation and evaporation cycle etc. In
159 order to measure the WP, the seasonal mean and maxima of SWH (of combined wind waves and
160 swell) and PWP are obtained from the six-hourly SWH and PWP data taken from ERA5.
161 Similarly, the seasonal mean SLP and SST were also derived from 6-hourly SLP and SST data of
162 ERA-5, respectively. In this study, the ERA5 reanalysis data for all the variables were
163 downloaded from the ECMWF website (<https://www.ecmwf.int/en/forecasts/datasets/reanalysis->

164 [datasets/era5/](#)) at a horizontal resolution of $0.5^{\circ} \times 0.5^{\circ}$ (i.e. SWH and PWP) or $0.25^{\circ} \times 0.25^{\circ}$ (i.e.,
165 SST and SLP).

166 **2.2. Climate Indices**

167 Indices used to represent climate variability associated with ENSO, IOD, and PDO over 1979–
168 2019 were obtained from several online sources. Overall, ENSO is the dominant coupled ocean–
169 atmosphere interaction occurring over the equatorial Pacific and significantly affects the
170 interannual climate variability globally (Collins et al. 2010; Stevenson 2012). In order to
171 examine the seasonal ENSO influence, the Niño-3.4 index (referred to as N34 herein) which
172 represents the average SST anomalies over the equatorial eastern Pacific (5°N – 5°S , 170°W –
173 120°W) was obtained from the National Oceanic and Atmospheric Administration/Climate
174 Prediction Center <http://www.cpc.ncep.noaa.gov/data/indices/>). To quantify the IOD impact, the
175 dipole mode index (DMI) was used (Saji et al., 1999; Webster et al., 1999), which is a measure
176 of the difference between the area-averaged SST anomalies in the western tropical Indian Ocean
177 (TIO) (50° – 70°E , 10°S – 10°N) and southeastern TIO (90° – 110°E , 10°S –Equator). Monthly SST
178 anomalies acquired from the extended Reconstructed Sea Surface Temperature (ERSST) dataset
179 to calculate the seasonal DMI index. The PDO index, prescribed as the principal mode of NP
180 monthly SST anomalies poleward of 20°N (Zhang et al., 1997), was obtained from the Joint
181 Institute for the Study of the Atmosphere and Ocean (JISAO) at the University of Washington
182 (<http://research.jisao.washington.edu/pdo/>).

183 Natural climate variability modes can interact with each other during different seasons (Cai et al.,
184 2011). Consequently, the independent influence of each should be considered when assessing the
185 impact of each mode. The seasonal correlation coefficients between the detrended N34 and DMI,

186 and N34 and PDO indices are shown in Table 2 for the period 1979–2019. A significant positive
 187 correlation (at the 1% level) between the N34 and PDO index is found during all seasons, with a
 188 range 0.397-0.545. For N34 and DMI indices, positive correlations only occur during JJA (i.e.
 189 0.312, p-value<0.05) and SON (0.620, p-value<0.01). The significant correlation between ENSO
 190 and IOD in JJA and SON suggests that IOD can be largely determined by ENSO and seasonally
 191 modulated responses, yet some IOD events can occur independently of ENSO events (Cai et al.
 192 2011; Kumar et al. 2019; Stucker et al. 2017). When analyzing the independent impact of each
 193 climate variability mode, the dependency of one climate variability index on the other is
 194 removed using linear regression analysis. For example, $ENSO|_{IOD}$ denotes the linearly
 195 independent residual ENSO index obtained after the removal of IOD from ENSO.

196

197 **2.3. Methodology**

198 **2.3.1. Derivation of Wave Power (WP)**

199 In essence, WP measures the transmission of energy by/through air-sea exchanges and used for
 200 wave motion (Donelan et al. 1997). For irregular waves, the total energy per unit area of water
 201 surface (in Joules/m²) is given as:

$$E = \rho g \int_0^{\infty} S(f) df, \tag{1}$$

203 where g is the acceleration due to gravity, ρ is the sea water mass density (~1028 kg/m³),
 204 $S(f)$ denotes the spectral density with respect to frequency f , and the n^{th} order moment is
 205 expressed in terms of spectral density as:

206
$$m_n = \int_0^{\infty} f^n S(f) df . \quad (2)$$

207 The SWH (H_s) and energy period (T_e) are computed from the integral of the spectral density and
 208 expressed in term of moment as follows:

209
$$H_s = 4\sqrt{m_0} \quad \text{and} \quad T_e = \frac{m_{-1}}{m_0} . \quad (3)$$

210 For each harmonic component of the wave spectrum, its energy travels at the group velocity
 211 defined by:

212
$$c_g(f, d) = \frac{1}{2} \sqrt{\frac{g}{k} \tanh(kd)} \left(1 + \frac{2kd}{\sinh(2kd)} \right) , \quad (4)$$

213 where d is the water depth, and k is the wave number which is related to the frequency f through
 214 the dispersion relation $(2\pi f)^2 = gk \tanh(kd)$. The total WP (also referred to as “wave energy
 215 flux”), in watts per meter (W/m) of wave crest width at any water depth d is given as

216
$$WP = \rho g \int_0^{\infty} c_g(f, d) S(f) df \quad (5)$$

217 On substituting equation (4) into equation (5) and using the dispersion relation:

218
$$WP = \frac{\rho g^2}{4\pi} \int_0^{\infty} \frac{S(f)}{f} \left[\left(1 + \frac{2k_f d}{\sinh(2k_f d)} \right) \tanh(k_f d) \right] df . \quad (6)$$

219 For large values of $k_f d$, the limits of \sinh and \tanh approaches to ∞ and 1, respectively. Thus,
 220 equation (6) reduces to:

221
$$WP = \frac{\rho g^2}{4\pi} \int_0^{\infty} \frac{S(f)}{f} df . \quad (7)$$

222 Substituting equations (2) and (3) into equation (7), WP is expressed as:

223
$$WP = \frac{\rho g^2}{4\pi} \left(\frac{T_e H_s^2}{16} \right) . \quad (8)$$

224 The energy period is estimated from the spectral shape and other parameters. When PWP (T_p) is
225 known, the energy period is estimated by using the following relation (Cornett, 2008):

226
$$T_e = \alpha T_p , \quad (9)$$

227 where α depends on the shape of the wave spectrum and α increases towards unity with
228 decreasing spectral width. Hagerman (2001) assumed $T_e=T_p$ in the assessment of the wave
229 energy resources over southern New England. In this study, the same assumption is adopted. On
230 substituting $T_e=T_p$ into equation (8), WP is expressed as:

231
$$WP = \frac{\rho g^2}{4\pi} \left(\frac{T_p H_s^2}{16} \right) . \quad (10)$$

232

233 **2.3.2. Generalized Extreme Value (GEV) Distribution**

234 Climate extremes are significant departures from the normal climate state and often have
235 widespread societal and ecological impacts. Thus, the correct representation of extreme events is
236 essential to understand their impacts. Extreme value theory provides the statistical description of
237 extremes in stationary and non-stationary processes. However, in the context of environmental

238 variables (e.g., SWH, temperature, precipitation), a non-stationary variable is used (Coles and
 239 Casson 1999; Gellens 2002; Nogaj et al. 2007; Kharin and Zwiers 2000, 2005), whereby extreme
 240 events are defined by three extreme value distributions, i.e., Gumbel distribution, Fréchet
 241 distribution, or Weibull distribution, arising from the limiting theorem of Fisher and Tippett
 242 (1928). The three distributions can be combined into a single form, the non-stationary GEV
 243 distribution, and its cumulative distribution function is given as:

$$244 \quad F(x, \mu_t, \sigma_t, \xi_t) = \begin{cases} \exp[-\exp(-\frac{x - \mu_t}{\sigma_t})], \xi_t = 0 \\ \exp[-(1 + \xi_t \frac{x - \mu_t}{\sigma_t})^{-\frac{1}{\xi_t}}], \xi_t \neq 0, 1 + \xi_t \frac{x - \mu_t}{\sigma_t} > 0 \end{cases}, \quad (11)$$

245 where $-\infty < \mu_t < \infty$, $\sigma_t > 0$, and $-\infty < \xi_t < \infty$ represent the location, scale, and shape
 246 parameters, respectively. For the non-stationary GEV distribution, the climate variability v_t
 247 (here, IOD, ENSO, and PDO indices, which are detrended and normalized) that varies with time
 248 (t) is used as a covariate of the GEV parameters. The location parameter (μ_t) as a function of
 249 climate variability is written as:

$$250 \quad \mu_t = \mu_0 + \mu_1(v_t - v_0), \quad (12)$$

251 where μ_0 represents the location parameter at time t_0 , and μ_1 denotes the regression coefficient
 252 representing the relationship between the climate variable and location parameter. Additionally,
 253 the scale and shape parameters can also be expressed as a function of climate variability as
 254 follows:

$$255 \quad \ln \sigma_t = \ln \sigma_0 + \sigma_1(v_t - v_0) \text{ and } \xi_t = \xi_0 + \xi_1(v_t - v_0), \quad (13)$$

256 where σ_0 and ξ_0 are the scale and shape parameter values at time t_0 , respectively, and σ_1 and ξ_1
257 are the corresponding regression coefficients. In order to examine the statistical significance of
258 climate variability on extremes, the log-likelihood ratio test is used. The log-likelihood test
259 compares the non-stationary GEV model with the stationary GEV model and assesses the GEV
260 parameters (Kharin and Zwiers 2005; Zhang et al. 2010).

261

262 **3. SST and SLP mean Teleconnection**

263 The patterns of seasonal mean SST and SLP regressed onto $\text{ENSO}|_{\text{IOD}}$, $\text{IOD}|_{\text{ENSO}}$, $\text{ENSO}|_{\text{PDO}}$, and
264 $\text{PDO}|_{\text{ENSO}}$ over the period 1979–2019 are shown in Fig.1 and regions with statistically significant
265 responses at the 5% level are indicated by hatching. Significant canonical responses in SST to
266 $\text{ENSO}|_{\text{IOD}}$ are evident over the eastern PO (warmer conditions during El Niño) and western PO
267 (colder conditions) throughout the year. In the IO, the strongest signals in SST are found over the
268 majority of the NIO and TIO in DJF and MAM, NIO in JJA, and NIO and western TIO in SON
269 (Fig. 1a). Further, the $\text{ENSO}|_{\text{IOD}}$ influence on SLP shows high and low pressure anomalies in
270 eastern and western regions of the southern Indo-Pacific Ocean, respectively, during DJF. This
271 anomalous pressure pattern generates strong winds over the southern Indo-Pacific Ocean, leading
272 to an enhancement in both SWH and PWP in DJF (Fig. 1b). Similarly, the Southern Oscillation
273 pattern of the coupled high and low pressure anomalies is also seen in DJF over the western and
274 eastern PO, respectively. This too presumably leads to both strong winds and enhances the wave
275 parameters (i.e., SWH and PWP) over the eastern PO (Fig. 1b). With the progression of the
276 seasons from DJF through to SON, the high and low pressure anomalies shift from the western
277 PO and eastern PO to central-western PO and eastern PO, respectively, during JJA and SON.

278 Additionally, high pressure anomalies are observed over the eastern parts of the SO, NIO, and
279 TIO, with low pressure anomalies over the central parts of the SO during MAM, JJA, and SON.
280 Such strong responses associated with SLP changes will also lead to strong responses in the
281 winds and wave parameters (Fig. 1b).

282 Significant impacts of $IOD|_{ENSO}$ on SST is predominantly confined to the western IO and AS in
283 DJF, which extend into parts of the tropical Pacific in MAM. During JJA and SON, the $IOD|_{ENSO}$
284 is associated with positive SST anomalies over the western-to-central IO in JJA and SON (Fig.
285 1a). The corresponding responses in SLP during DJF show high pressure anomalies over most of
286 the tropical and mid-latitude region of the Indo–Pacific Ocean, and low pressure anomalies over
287 the AS and high-latitude region of the Indo–Pacific Ocean. In MAM, the $IOD|_{ENSO}$ influence is
288 most significant over the mid-to-high latitudes in both hemispheres. In JJA, high SLP anomalies
289 expand over the mid-latitudes of Indo-Pacific Ocean, from the eastern IO to central PO, and low
290 pressure anomalies strengthen and expand over the western IO. In SON, high SLP anomalies are
291 evident over the eastern IO and tropical PO, and develop over the eastern southern PO, whereas
292 the low pressure anomalies over the western IO are similar to JJA. Such high and low SLP
293 anomalies, with progressing seasonal patterns, will consequently produce strong winds and
294 consequently enhance the wave parameters in the respective regions (Fig. 1b).

295 The $ENSO|_{PDO}$ impact closely resembles that of $ENSO|_{IOD}$ whereby warmer SSTs are evident
296 over the eastern PO and colder SST over the western PO year around (*c.f.* first and third rows in
297 Fig 1a). In the IO, significant positive signals in SST due to $ENSO|_{PDO}$ are again evident over
298 large parts of the NIO and TIO in most seasons, being weakest in JJA (Fig. 1a). Further, the
299 $ENSO|_{PDO}$ influence on SLP is also consistent with that of $ENSO|_{IOD}$ whereby the significant
300 signals being associated with the widespread high and low pressure anomalies over the western

301 and eastern Indo-Pacific Ocean, respectively (*c.f.* first and third rows in Fig. 1b). However, high
302 pressure anomalies are subdued in the western IO during SON for $ENSO|_{PDO}$ compared to that
303 associated with $ENSO|_{IOD}$. Thus, the above changes of both $ENSO|_{IOD}$ and $ENSO|_{PDO}$ are likely
304 to generate the similar variations in the generated winds and wave fields in the respective
305 regions, except for the western IO.

306 The independent PDO influence (i.e., $PDO|_{ENSO}$) on SST is observed to induce consistent year-
307 round pattern with long-term SST increases (warm SST) over the eastern PO (extending towards
308 the west along the equator) and decreases (cold SST) over the western NP and southwest tropical
309 PO (Fig. 1a). This represents the typical pattern associated with a positive PDO. In the IO, the
310 strong $PDO|_{ENSO}$ influences on SST occur over the AS in MAM, NIO and SCP seas in JJA, and
311 BOB and SCP seas in SON (Fig. 1a). The corresponding responses in SLP exhibit an anomalous
312 low pressure over the north and tropical Pacific and an anomalous high pressure over the eastern
313 TIO in DJF (Fig. 1b). In addition, anomalous high and low pressure centers are evident over the
314 south Pacific in DJF. In MAM, positive responses in SLP to the $PDO|_{ENSO}$ are observed over the
315 large section of the tropical and mid-latitude region of the Indo-Pacific Ocean, with counter
316 responses (low-pressure anomalies) over high latitudes of the Indo-Pacific Ocean. In JJA, the
317 $PDO|_{ENSO}$ influence on SLP is most significant over the western Pacific Ocean (PO)
318 (high-pressure anomalies) and eastern NP and Southern Ocean (SO) (low-pressure anomalies).
319 These anomalies propagate into the western NP (high-pressure anomalies) and central NP
320 (low-pressure anomalies) in SON. In SON, high and low pressure anomalies are evident over the
321 SO.

322

323

324 **4. Influence of Indo-Pacific Climate Variability**

325 **4.1. ENSO Influence**

326 Spatial patterns of the seasonal mean and extreme WP (WPavg and WPmax), SWH (Havg and
327 Hmax), and PWP (Pavg and Pmax) responses to independent ENSO_{|IOD} influence (i.e. the
328 independent ENSO influence obtained after the removal of IOD signals) over the period 1979–
329 2019 in the Indo–Pacific Ocean are shown in Fig. 2. In addition, the original seasonal ENSO
330 influence (i.e., no removal of covarying IOD signals) on the mean and extreme WP, SWH, and
331 PWP is also provided in Supplementary Fig. 1 to assess the role of IOD in strengthening and
332 weakening the ENSO impact. Overall, mean responses in WPavg, Havg, and Pavg were acquired
333 by using linear regression whereas extreme responses in WPmax, Hmax, and Pmax were based
334 on the non-stationary GEV analysis. Regions with statistically significant responses at the 5%
335 level are indicated by hatching.

336 Widespread positive responses in WPmax to ENSO_{|IOD} are evident over the eastern Pacific and
337 southern part of the IO (an extension from south of Australia) in DJF (Fig. 2a). As the seasons
338 progress from DJF through to SON, large seasonal variations in WP are observed in both the IO
339 and PO. In the PO, positive amplitudes of the WPmax occur more over the central Pacific in
340 MAM, which shift further towards the western Pacific in JJA and SON (Fig. 2a). The strong
341 increases in extreme WP in the western NP and BOB during JJA, and in the western NP during
342 SON, presumably arises from the enhanced tropical cyclone activities during that time of year
343 (Shanas and Kumar 2014; Yang and Oh 2020, 2018; Zhan et al. 2011). However, WPmax
344 exhibit larger seasonality in the IO compared to the PO. For example, the WP increases over the
345 western TIO in MAM, over the western TIO, BOB, SCP seas in JJA, and over the eastern TIO

346 during SON in response to $ENSO|_{IOD}$ (Fig. 2a). The regression patterns of $ENSO|_{IOD}$ on mean
347 WP are similar to the extreme. Consistently, the $ENSO|_{IOD}$ influence on H_{avg} and H_{max} over the
348 Indo-Pacific Ocean (Fig. 2b) shows similar seasonal and regional variations as WP_{avg} and
349 WP_{max} , due to SWH being a dominating factor in determining the WP (Bromirski et al. 2005,
350 2013; Reguero et al. 2019; Yang and Oh 2020). Lastly, the impact of $ENSO|_{IOD}$ on P_{avg} and
351 P_{max} is found to be largest over the eastern PO in DJF and over the western PO in JJA and SON
352 (Fig 2c). Such regions exhibit a significant relationship, whereby changes to tropical SST
353 anomalies due to the warm ENSO phase resulted in variations in anomalous long PWP. In the IO
354 however, significant increases in P_{avg} and P_{max} are observed over large parts of the IO year-
355 round due to $ENSO|_{IOD}$, but more so in DJF and MAM (Fig. 2c).

356 Comparing independent ENSO influences ($ENSO|_{IOD}$) to the original ENSO signals (*c.f.* Fig. 2
357 and Supplementary Fig. 1), it is found that WP_{avg} is enhanced more over the eastern TIO in JJA
358 and SON, and over the central NP in SON for the independent ENSO influence. This indicates
359 that the IOD acts to reduce the ENSO impact in these regions during JJA and SON. In addition,
360 enhancement in the independent ENSO influence is also exhibited in the mean and extreme
361 SWH responses when the covarying IOD signal is removed during JJA and SON (*c.f.* Fig. 2b and
362 Supplementary Fig. 1b). However, positive responses in mean and extreme PWP associated with
363 ENSO in the IO are significantly reduced during SON when the covarying IOD signal is
364 removed (*c.f.* Fig 2c and Supplementary Fig. 1c). In DJF and MAM, the $ENSO|_{IOD}$ impact on
365 mean and extreme WP, SWH, and PWP exhibits similar regional variations as observed for the
366 complete ENSO signals as the IOD is not active during these seasons.

367 **4.2. IOD Influence**

368 Seasonal spatial regression patterns of mean and extreme WP, SWH, and PWP against the
369 independent IOD influence (denoted as $IOD|_{\text{ENSO}}$) after removing the ENSO signal over 1979–
370 2019 in the Indo-Pacific Ocean are presented in Fig. 3. Further, the original seasonal IOD
371 influence (here using the DMI) on the mean and extreme WP, SWH, and PWP that include
372 variability due to ENSO is also provided in Supplementary Fig. 2.

373 Statistically significant $IOD|_{\text{ENSO}}$ influences on WP_{avg} and H_{avg} are limited in the Indo-Pacific
374 Ocean and are generally less intense than ENSO influences (*c.f.* Fig. 2 and Fig.3). During DJF
375 and MAM, the positive responses of extreme WP and SWH to $IOD|_{\text{ENSO}}$ are evident over the SO,
376 and the responses extend into the IO for PWP (Fig 3). Significantly decreased signals are also
377 found over the AS and central-to-western IO during MAM. However, the IOD is not active
378 during this half of the year; therefore, such signals may be related to other variability intrinsic to
379 the IO, such as the Indian Ocean Basin Mode (IOBM), which are shown to prolong ENSO
380 effects (Yuan et al. 2008). During JJA and SON, decreases in WP and SWH are evident over the
381 majority of the eastern IO, with increases only in extremes in the BOB in JJA (related to
382 increased cyclonic activity), and over the AS and southwestern IO in SON (Fig. 3a-b). The
383 opposite occurs for mean and extreme PWP, where weak decreases are found over the entire IO
384 in JJA, but large increases are found over the eastern IO alongside decreases over the western IO
385 in SON. The $IOD|_{\text{ENSO}}$ influence on extreme WP and SWH is evident over the eastern PO in DJF,
386 over the central north Pacific in MAM, over the western PO in JJA and SON (Fig. 3a,-b). The
387 mean responses to $IOD|_{\text{ENSO}}$ are also observed to follow similar patterns as the extreme, except
388 for the western PO and BOB in JJA. The western PO and BOB are subject to high WP due to
389 intensified tropical cyclone activity during JJA (Shanas and Kumar 2014; Yang and Oh 2020,

390 2018); however, negative amplitudes in these regions suggest that El Niño hampers such activity
391 and resulting in smaller WP.

392 Overall, an increase in SWH and decrease in PWP over regions such as the BOB and the north-
393 western Australian coast in DJF are associated with the seasonal increase in small fetch winds
394 (Remya et al. 2020). In addition, significant impact of the $IOD|_{ENSO}$ on SWH is constrained to
395 the eastern IO and BOB in JJA, with decreases in mean PWP. This indicates that whilst swells
396 dominate the IO, wind seas (directly generated and strongly coupled to local winds) are also of
397 importance in JJA during positive IOD events (Remya et al., 2020). In SON, the strongest
398 $IOD|_{ENSO}$ responses in PWP are evident over the entire IO, except the far western IO. However,
399 in the PO, positive responses of PWP to $IOD|_{ENSO}$ occur over the eastern PO except in SON,
400 where decreases in PWP occur over the majority of the PO (Fig.3c).

401 Lastly, comparing independent IOD influences ($IOD|_{ENSO}$) to the original IOD signals (*c.f.* Fig. 3
402 and Supplementary Fig. 2), the independent IOD impacts on WP, SWH, and PWP are similar to
403 the complete IOD signal, yet slightly reduced over the entire Indo–Pacific Ocean in DJF and
404 MAM, and over the IO during SON. This emphasizes the significant influence of the IO climate
405 variability over the Indo–Pacific Ocean in DJF and MAM, and over the IO in SON even in the
406 absence of ENSO. In the PO, decreases in WP_{avg} and H_{avg} over the western NP in JJA and
407 SON occur, indicating that ENSO plays a vital role in enhancing the IOD influences in this
408 region (*c.f.* Fig. 3a-b and Supplementary Fig. 2a-b). Similarly, the negative responses of P_{avg} to
409 $IOD|_{ENSO}$ are evident over the western NP in JJA and SON, yet they are positive when the
410 covarying ENSO influence is included. This suggests that the PWP signals in the western NP are
411 significantly subdued when the IOD and ENSO are in phase (*c.f.* Fig. 3c and Supplementary Fig.
412 2c).

413 4.3. PDO Influence

414 Seasonal regression patterns of WPavg and WPmax, Havg and Hmax, and Pavg and Pmax
415 against the $\text{ENSO}|_{\text{PDO}}$ (i.e., ENSO independent of the PDO variability) and $\text{PDO}|_{\text{ENSO}}$ (i.e., PDO
416 independent of the covarying ENSO signals) over 1979–2019 in the Indo-Pacific Ocean are
417 displayed in Figs. 4 and 5, respectively. In addition, the original ENSO and PDO influence on
418 the mean and extreme WP, SWH, and PWP are also provided in supplementary Fig. 1 and Fig. 3,
419 respectively.

420 Overall, the $\text{ENSO}|_{\text{PDO}}$ influence on mean WP exhibits similar regional and seasonal variations
421 as in the original ENSO but with a slight reduction in the amplitude throughout the year, apart
422 from the PO in MAM, indicating the dominant impact of ENSO even in the absence of PDO (*c.f.*
423 Fig. 4a and Supplementary Fig. 1a). In MAM, a decrease in WPavg is evident over the central
424 Pacific. This reveals that PDO enhances the WP over the central Pacific in MAM (*c.f.* Fig. 4a
425 and Supplementary Fig. 1a). The impact of the $\text{ENSO}|_{\text{PDO}}$ on WPmax is similar to WPavg yet
426 with stronger amplitudes. The regression patterns of mean and extreme SWH associated with the
427 $\text{ENSO}|_{\text{PDO}}$ are also consistent with the regression patterns of mean and extreme WP throughout
428 the year (Fig. 4b). Further, the Pavg and Pmax response patterns to $\text{ENSO}|_{\text{PDO}}$ are similar to
429 those of the original ENSO year-round except in MAM. In MAM, a reduction in response
430 patterns of Pavg and Pmax to $\text{ENSO}|_{\text{PDO}}$ over the central NP (Fig. 4c) is associated with the SST
431 changes driven by the PDO (Fig. 1a).

432 For the independent PDO influence (i.e. $\text{PDO}|_{\text{ENSO}}$), significant increases in mean and extreme
433 WP and SWH are mostly confined to the PO and most prominent in the NP (Fig. 5a-b). Over the
434 IO, positive $\text{PDO}|_{\text{ENSO}}$ responses in WP and SWH are most prevalent during JJA. However,

435 strong counter responses (i.e. significant decreases in WPavg and Havg) are evident over the
436 same regions during SON (Fig. 5a-b). Overall, the extreme responses to $\text{PDO}|_{\text{ENSO}}$ for WP and
437 SWH are consistent with those of the mean responses. The strongest impact of independent PDO
438 (i.e. $\text{PDO}|_{\text{ENSO}}$) on Pavg and Pmax is observed over the central NP in DJF and SON, and over the
439 eastern and southern PO in MAM and JJA (Fig. 5c). This suggests that enhanced PWP in these
440 regions are related to the SST changes associated with positive PDO phase (Fig. 1a). In DJF and
441 MAM, PWP decreases and SWH increases in the western NP are related to the seasonal increase
442 in wind seas. In the IO, positive responses to $\text{PDO}|_{\text{ENSO}}$ in Pavg and Pmax are evident over the
443 mid-latitudes of the SIO in DJF, and over the western IO in MAM. In JJA, an increase in Pavg
444 and Pmax values occurs over the entire IO apart from a small part of the western SIO.
445 Conversely, counter responses in Pavg and Pmax (i.e. decreases over the IO) are found in SON.

446 Lastly, comparing the seasonal PDO influence independent of ENSO (i.e., $\text{PDO}|_{\text{ENSO}}$) to the
447 original PDO signals (*c.f.* Fig. 5 and Supplementary Fig. 3), it is evident that excluding the co-
448 occurring ENSO signals from PDO reduces the response amplitudes over the eastern PO and
449 mid-latitudes of the SIO in DJF, western TIO, and SIO in MAM, western PO in JJA, and western
450 PO and SIO in SON. This reveals that ENSO plays a significant role in enhancing PDO
451 influences in these regions during these seasons. However, enhanced WP also occurs over the
452 western PO in MAM and the eastern Pacific in JJA (*c.f.* Fig. 5 and Supplementary Fig. 3).

453 **5. Composite Analysis**

454 **5.1. Composite Analysis of ENSO and IOD**

455 As various natural climate variabilities modes interact with one another in a particular season.
456 So, the independent influence of ENSO, IOD, and PDO is analyzed above (in section 4). To get

457 further insight into the interrelation between the various modes of natural climate variability, the
458 composite analysis of the mean and extreme WP for different ENSO and IOD, and ENSO and
459 PDO phase combinations is conducted for the 41 year period over the Indo – Pacific Ocean. In
460 this section composite analysis is conducted between ENSO and IOD. For this, El Niño
461 (ENSO+), La Niña (ENSO–), and positive and negative IOD (pIOD and nIOD, respectively)
462 years are chosen from the detrended and normalized time series of the original indices for those
463 values where ENSO and IOD indices exceeded a threshold value of ± 0.5 (list of the years is
464 provided in Table. 3). This gives a total of 9, 3, 5, and 9 sample years in JJA and 11, 3, 4, and 12
465 sample years in SON for the combination of El Niño/pIOD, La Niña/pIOD, El Niño/nIOD, and
466 La Niña/nIOD, respectively. The composite patterns of (left panel) mean and (right panel)
467 extreme WP anomalies in (a) JJA and (b) SON for various ENSO and IOD combinations are
468 shown in Fig. 6.

469 The WPavg and WPmax increases during the El Niño/pIOD years and decreases during La
470 Niña/nIOD years over the western PO, BOB, western TIO, and western SIO in JJA and over the
471 western PO in SON (Fig. 6a and b). The combination of an El Niño event with a pIOD (or nIOD)
472 leads to increase in mean and extreme WP over the western NP and counter response is evident
473 for the combination of La Niña with pIOD (or nIOD) in JJA and SON, reveals the strengthening
474 of ENSO in enhancing/reducing WP in western NP (Fig. 6a and b). During out – phase
475 combinations (i.e. El Niño/nIOD and La Niña/pIOD), an increase in mean and extreme WP is
476 observed over the south-east Indo – Pacific Ocean during La Niña/pIOD and decrease during El
477 Niño/nIOD in JJA and SON.

478 **5.2. Composite Analysis of ENSO and PDO**

479 The composite patterns of (left panel) mean and (right panel) extreme WP anomalies in (a) DJF,
480 (b) MAM, (c) JJA, and (d) SON for various ENSO and PDO combinations are displayed in Fig.
481 7. For composite analysis, El Niño (ENSO+), La Niña (ENSO-), and positive and negative PDO
482 (pPDO and nPDO, respectively) years are chosen from the detrended and normalized time series
483 of the original indices for those values where ENSO and PDO indices exceeded a threshold value
484 of ± 0.5 (list of the years is provided in Table. 4). This yields a total of 8, 5, 2, and 8 sample years
485 in DJF, 13, 5, 3, and 11 sample years in MAM, 7, 3, 6, and 8 sample years in JJA, and 12, 5, 2,
486 and 12 sample years in SON for the combination of El Niño/pPDO, La Niña/pPDO, El
487 Niño/nPDO, and La Niña/nPDO, respectively.

488 For El Niño/pPDO events, WPavg increases over the eastern PO in DJF, the central NP in
489 MAM, NPO, SIO, BOB, and western TIO in JJA, and western PO in SON and decreases over
490 the NIO, TIO, SCP seas, and western NP in DJF, western NP and eastern SPO in MAM and JJA,
491 and in the eastern PO, NIO, and TIO and its counter responses are observed during La
492 Niña/nPDO (Fig. 7, left panel). In SIPO and PO apart from the coastal regions of the western
493 NP, an El Niño (La Niña) event with a pPDO leads to a significant increase (decrease) in WPavg
494 in DJF (Fig. 7a, left panel). The increase in WPavg is seen over the larger parts of the NIO and
495 TIO in MAM during in-phase combinations (i.e., El Niño/pPDO or La Niña/nPDO) (Fig. 7b, left
496 panel). In western NP, WPavg increases for the combination of El Niño with a pPDO (or nPDO)
497 and decreases for the combination of La Niña with a pPDO (or nPDO) in JJA and SON. This
498 reveals that ENSO is responsible for enhancing/subsiding the WP over the western NP in JJA
499 and SON. Further, a La Niña event associated with pPDO, enhances the WPavg over the IO
500 while, the counter responses are evident for the combination of a La Niña with nPDO in JJA.
501 The combination of an El Niño (or a La Niña) with pPDO, decreases the mean WP over the

502 larger parts of the IO, while increases for the combination of an El Niño (or a La Niña) with
503 nPDO in SON. When ENSO and PDO are in out phase combinations (i.e. El Niño/nPDO and La
504 Niña/pPDO), the patterns are noisy and even change the sign in DJF, depicts a decrease in WP
505 over the larger parts of the Indo – Pacific Ocean in MAM, and an increase in WPavg over the
506 BOB and western TIO and decrease in WPavg over the eastern PO in JJA. In SON, an enhance
507 in WPavg is observed over the larger parts of the IO, western PO and mid-latitudes of the SPO
508 during El Niño/nPDO events and decreases during La Niña/pPDO (Fig. 7d). The impact of the
509 ENSO and PDO combinations on extreme WP extreme appears over the same region as in the
510 mean WP year around (Fig. 7, right panel).

511 **6. Summary and Conclusions**

512 This study investigates the impact of natural climate variability modes such as ENSO, IOD, and
513 PDO on seasonal extreme WP in the Indo-Pacific Ocean using ERA5 reanalysis data over the
514 period 1979–2019. A non-stationary GEV distribution is applied on the seasonal extremes to
515 determine the regions with significant impact, where the natural climate variability modes are
516 taken as the covariates. In addition, the response patterns of SWH, PWP, SST, and SLP to
517 climate variability modes are also evaluate to understand the underlying physical mechanism
518 involved in increasing (or decreasing) the WP. Overall, the strongest ENSO|IOD influence on
519 extreme WP is evident over the eastern Pacific and southern part of the IO (an extension from
520 south of Australia) in DJF, the central Pacific and western TIO in MAM, the western Pacific,
521 western TIO, BOB, SCP seas in JJA, and the western Pacific and eastern TIO in SON. The
522 positive responses of extreme WP to IOD|ENSO are observed over the eastern PO and SO in DJF,
523 the central north Pacific and SO in MAM, the western PO and BOB in JJA, and the southwestern
524 IO in SON whereas, significantly decreased signals are found over the AS and central-to-western

525 IO during MAM and the western PO in SON. The $ENSO|_{PDO}$ influence on extreme WP exhibits
526 similar regional and seasonal variations as in the original ENSO but with a slight reduction in the
527 amplitude throughout the year apart from the PO in MAM. For the $PDO|_{ENSO}$ influence,
528 significant increases in extreme WP are mostly confined to the PO and most prominent in the
529 NP. Over the IO, positive $PDO|_{ENSO}$ responses in WP are most prevalent during JJA and over the
530 SIO and eastern IO.

531 The independent seasonal influence of each climate mode on mean and extreme WP, SWH, and
532 PWP was compared with the original to assess the role of one variability mode in strengthening
533 or weakening the influence of another variability mode. The ENSO influence on extreme WP,
534 independent of IOD, exhibits enhanced WPmax over the eastern TIO in JJA and over the eastern
535 TIO and central NP in SON compared to the original ENSO signals. This implies that the IOD
536 reduces the ENSO signals in these regions during that time of year. The independent IOD impact
537 on WP shows a decrease in WPmax over the western NP in JJA and more so in SON. This
538 suggests that ENSO plays an important role in enhancing the IOD influence in this region during
539 JJA and SON. The independent ENSO influence on WPmax, obtained after the removal of PDO,
540 reveals that the PDO has little to no influence over ENSO signals in the Indo–Pacific Ocean
541 except in MAM. In MAM, the PDO has a strong impact over the influence of ENSO in the PO.
542 Lastly, the independent PDO impact, after removing the ENSO signals, is related to a decrease in
543 WPmax over the eastern PO in DJF, and western NP in JJA and SON. This demonstrates that
544 ENSO is responsible for increasing the WP in these regions during that time of the year. In
545 MAM, ENSO reduces the PDO signals over the PO. In addition, seasonal SLP teleconnection
546 patterns regressed against $ENSO|_{IOD}$, $IOD|_{ENSO}$, $ENSO|_{IOD}$, and $PDO|_{ENSO}$, exhibit a high and low
547 pressure anomaly that in turn generates strong winds (Kumar et al 2016, 2019; Patra et al. 2020;

548 Remya et al., 2020; Yang and Oh 2018) and consequently enhances the wave parameters (i.e. Hs
549 and Tp) in the respective localized regions. Overall, the mean WP patterns were highly
550 correlated with the extreme WP patterns year-round. Maximum WP increases were often found
551 during seasons when there are increases in tropical cyclone activity and strong winds, such as
552 NIO during JJA.

553 Composite analysis of mean and extreme WP for the different phase combinations of natural
554 climate variabilities (i.e. ENSO with IOD and ENSO with PDO) strengthen the conclusions
555 drawn from the independent influence patterns (i.e. ENSO, IOD, and PDO separately), which
556 shows that the IOD (or PDO) plays an important role in enhancing or reducing the intensity of
557 ENSO-related responses, or vice versa, depending on the season. During JJA, the IOD enhances
558 (reduces) the ENSO impact on WP when both are in-phase (out-phase) combinations. In SON,
559 (i.e., when ENSOs generally develop and IODs reaches in its mature phase), ENSO is able to
560 enhance the IOD influence on WPavg and WPmax significantly. While, PDO (i.e. pPDO or
561 nPDO events) enhances (reduces) the ENSO influence on WP during El Niño (La Niña) year-
562 round.

563 **Acknowledgements**

564 All the data (SWH, PWP, SST, and SLP) used in this manuscript is obtained from ERA5
565 reanalysis from the ECMWF website ([https://www.ecmwf.int/en/forecasts/datasets/reanalysis-](https://www.ecmwf.int/en/forecasts/datasets/reanalysis-datasets/era5)
566 [datasets/era5](https://www.ecmwf.int/en/forecasts/datasets/reanalysis-datasets/era5)). We would like to acknowledge the working groups for the development of the
567 ERA5 reanalysis datasets. In addition, the current research is supported by Ministry of Earth
568 Sciences (MoES), Government of India and Department of Applied Sciences, National Institute
569 of Technology Delhi.

570

571

572 **References**

573 Aarnes, O. J., Abdalla, S., Bidlot, J.-R., & Breivik, Ø. (2015). Marine wind and wave height trends
574 at different ERA-Interim forecast ranges. *J. Climate*, 28 (2), 819–

575 837. <https://doi.org/10.1175/JCLI-D-14-00470.1>

576 Allan, J.C., & Komar, P.D. (2006). Climate controls on US West Coast erosion processes. *Journal*
577 *of coastal research*, 22 (3), 511-529. <https://doi.org/10.2112/03-0108.1>

578 Amrutha, M.M., Kumar, V.S., Bhaskaran, H., & Naseef, M. (2019). Consistency of wave power at
579 a location in the coastal waters of central eastern Arabian Sea. *Ocean Dynamics*, 69(5), 543–

580 560. <https://doi.org/10.1007/s10236-019-01267-1>

581 Amrutha, M.M., & Kumar, V.S. (2020). Changes in Wave Energy in the Shelf Seas of India
582 during the Last 40 Years Based on ERA5 Reanalysis Data. *Energies*, 13(1),

583 115. <https://doi.org/10.3390/en13010115>

584 Arinaga, R.A., & Cheung, K.F. (2012). Atlas of global wave energy from 10 years of reanalysis
585 and hindcast data. *Renewable Energy*, 39(1), 49-64. <https://doi.org/10.1016/j.renene.2011.06.039>

586 Aydoğan, B., Ayat, B., & Yüksel, Y. (2013). Black Sea wave energy atlas from 13 years
587 hindcasted wave data. *Renewable energy*, 57, 436–

588 447. <https://doi.org/10.1016/j.renene.2013.01.047>

589 Barstow, S., Mørk, G., Mollison, D., & Cruz, J. (2008). The wave energy resource. In J. Cruz
590 (Eds.), *Ocean wave energy* (pp. 93-132). Springer.

591 Bromirski, P.D., Cayan, D.R.,& Flick, R.E. (2005). Wave spectral energy variability in the
592 northeast Pacific. *Journal of Geophysical Research: Oceans*, 110(C3).<https://doi.org/10.1029/2004JC002398>
593
594 Bromirski, P.D.,&Kossin, J.P. (2008). Increasing hurricane wave power along the US Atlantic
595 and Gulf coasts. *Journal of Geophysical Research: Oceans*, 113(C7).<https://doi.org/10.1029/2007JC004706>
596
597 Bromirski, P.D., & Cayan, D.R. (2015). Wave power variability and trends across the
598 NorthAtlantic influenced by decadal climate patterns. *Journal of Geophysical Research: Oceans*, 120(5), 3419-3443.<https://doi.org/10.1002/2014JC010440>
599
600 Bromirski, P.D., Cayan, D.R., Helly, J.,&Wittmann, P. (2013). Wave power variability and
601 trends across the North Pacific. *Journal of Geophysical Research: Oceans*, 118(12), 6329-
602 6348.<https://doi.org/10.1002/2013JC009189>
603
604 Caires, S., Swail, V. R.,& Wang, X. L. (2006). Projection and analysis of extreme wave
605 climate. *J. Climate*, 19 (21), 5581-5605. <https://doi.org/10.1175/JCLI3918.1>
606
607 Cai, W., Sullivan, A.,& Cowan, T.(2011). Interactions of ENSO, the IOD, and the SAM in
608 CMIP3 models. *J. Climate*, 24 (6), 1688-1704.<https://doi.org/10.1175/2010JCLI3744.1>
609
610 Carter, D.J.T.,& Draper, L. (1988). Has the north-east Atlantic become
611 rougher? *Nature*, 332(6164), 494-494.<https://doi.org/10.1038/332494a0>
612
613 Chen, G., Chapron, B., Ezraty, R.,&Vandemark, D. (2002). A global view of swell and wind sea
614 climate in the ocean by satellite altimeter and scatterometer. *Journal of Atmospheric and
615 Oceanic Technology*, 19(11), 1849-1859.[https://doi.org/10.1175/1520-0426\(2002\)019%3C1849:AGVOSA%3E2.0.CO;2](https://doi.org/10.1175/1520-0426(2002)019%3C1849:AGVOSA%3E2.0.CO;2)

613 Coles SG (2001) An introduction to statistical modeling of extreme values. Springer, London, p
614 225. <https://doi.org/10.1007/978-1-4471-3675-0>

615 Coles, S., & Casson, E. (1999). Extreme value modelling of hurricane wind speeds. *Structural*
616 *Safety*, 20(3), 283-296. [https://doi.org/10.1016/S0167-4730\(98\)00015-0](https://doi.org/10.1016/S0167-4730(98)00015-0)

617 Collins, M., An, S. I., Cai, W., Ganachaud, A., Guilyardi, E., Jin, F. F., et al. (2010). The impact
618 of global warming on the tropical Pacific Ocean and El Niño. *Nature Geoscience*, 3(6), 391–397.
619 <https://doi.org/10.1038/ngeo868>.

620 Dee, D. P., Uppala, S.M., Simmons, A.J., Berrisford, P., Poli, P., Kobayashi, S., et al. (2011). The
621 ERA-Interim reanalysis: Configuration and performance of the data assimilation system.
622 *Quarterly Journal of the royal meteorological society*, 137(656), 553–597. doi:10.1002/qj.828

623 .

624 Donelan, M.A., Drennan, W.M., & Katsaros, K.B. (1997). The air–sea momentum flux in
625 conditions of wind sea and swell. *Journal of physical oceanography*, 27(10), 2087-
626 2099. [https://doi.org/10.1175/1520-0485\(1997\)027%3C2087:TASMF1%3E2.0.CO;2](https://doi.org/10.1175/1520-0485(1997)027%3C2087:TASMF1%3E2.0.CO;2)

627 Fan, Y., Lin, S.J., Held, I.M., Yu, Z., & Tolman, H.L. (2012). Global ocean surface wave
628 simulation using a coupled atmosphere–wave model. *Journal of Climate*, 25(18), 6233-
629 6252. <https://doi.org/10.1175/JCLI-D-11-00621.1>

630 Feng, X., Tsimplis, M., & Yelland, M. (2012). Extreme waves at the polar front of North
631 Atlantic from 2000 to 2009 (p. 5719). EGU General Assembly 2012, Vienna, Austria

632 Fisher, R. A., & Tippett, L. H. C. (1928). Limiting forms of the frequency distributions of the
633 largest or smallest members of a sample. *Proceedings of the Cambridge Philosophical Society*,
634 24, 180–190.

635 Gellens, D. (2002). Combining regional approach and data extension procedure for assessing
636 GEV distribution of extreme precipitation in Belgium. *Journal of Hydrology*, 268(1-4), 113-126.

637 Gulev, S. K., & Grigorieva, V. (2004). Last century changes in ocean wind wave height from
638 global visual wave data. *Geophysical Research Letters*, 31(24), L24302.
639 <https://doi.org/10.1029/2004GL021040>

640 Gulev, S.K., & Grigorieva, V. (2006). Variability of the winter wind waves and swell in the North
641 Atlantic and North Pacific as revealed by the voluntary observing ship data. *Journal of*
642 *Climate*, 19(21), 5667-5685. <https://doi.org/10.1175/JCLI3936.1>

643 Gunn, K., & Stock-Williams, C. (2012). Quantifying the global wave power resource. *Renewable*
644 *Energy*, 44, 296-304. <https://doi.org/10.1016/j.renene.2012.01.101>

645 Hagerman, G. (2001). Southern New England Wave Energy Resource Potential. Proc. Building
646 Energy 2001, Boston, USA.

647 Hersbach, H., & Dee, D. (2016). ERA5 reanalysis is in production. ECMWF Newsletter, 147.
648 https://www.ecmwf.int/en/newsletter/147/news/35_era5-reanalysis-production (last access: 14
649 November 2018)

650 Hemer MA, Church JA, Hunter JR (2010) Variability and trends in the directional wave climate
651 of the Southern Hemisphere. *Int J Climatol* 30:475–491. <https://doi.org/10.1002/joc.1900>

652

653 Hemer, M.A., Simmonds, I., & Keay, K. (2008). A classification of wave generation
654 characteristics during large wave events on the Southern Australian margin. *Continental Shelf*
655 *Research*, 28(4-5), 634-652. <https://doi.org/10.1016/j.csr.2007.12.004>

656 Hemer, M.A., Manasseh, R., McInnes, K.L., Penesis, I., & Pitman, T. (2018). Perspectives on a
657 way forward for ocean renewable energy in Australia. *Renewable Energy*, *127*, 733-
658 745. <https://doi.org/10.1016/j.renene.2018.05.036>

659 Hemer, M.A., Zieger, S., Durrant, T., O'Grady, J., Hoeke, R.K., McInnes, K.L., & Rosebrock, U.
660 (2016). A revised assessment of Australia's national wave energy resource. *Renewable*
661 *Energy*, *114*, 85-107. <https://doi.org/10.1016/j.renene.2016.08.039>

662 Hulls, K. (1977). Wave power. *New Zealand Energy Journal*, *4*, 44–48.

663 Izaguirre, C., Méndez, F.J., Menéndez, M., & Losada, I.J. (2011). Global extreme wave height
664 variability based on satellite data. *Geophysical Research*
665 *Letters*, *38*(10), L10607. doi:10.1029/2011GL047302

666 Izaguirre, C., Méndez, F. J., Menéndez, M., Luceño, A., & Losada, I. J. (2010). Extreme wave
667 climate variability in southern Europe using satellite data. *Journal of Geophysical*
668 *Research: Oceans*, *115*, C04009. <https://doi.org/10.1029/2009JC005802>.

669 Kharin, V.V., & Zwiers, F.W. (2000). Changes in the extremes in an ensemble of transient climate
670 simulations with a coupled atmosphere–ocean GCM. *Journal of Climate*, *13*(21), 3760-
671 3788. [https://doi.org/10.1175/1520-0442\(2000\)013%3C3760:CITEIA%3E2.0.CO;2](https://doi.org/10.1175/1520-0442(2000)013%3C3760:CITEIA%3E2.0.CO;2)

672 Kharin, V. V., & Zwiers, F. W. (2005). Estimating extremes in transient climate change
673 simulations. *Journal of Climate*, *18*(8), 1156–1173. <https://doi.org/10.1175/JCLI3320.1>

674 Kumar, P., Kaur, S., Weller, E., & Min, S.K. (2019). Influence of Natural Climate Variability on
675 the Extreme Ocean Surface Wave Heights Over the Indian Ocean. *Journal of Geophysical*
676 *Research: Oceans*, *124*(8), 6176-6199. <https://doi.org/10.1029/2019JC015391>

677 Kumar, P., Min, S. K., Weller, E., Lee, H., & Wang, X. L. (2016). Influence of climate
678 variability on extreme ocean surface wave heights assessed from ERA-interim and ERA-20C.
679 *Journal of Climate*, 29(11), 4031–4046. <https://doi.org/10.1175/JCLI-D-15-0580.1>

680 Kumar, V.S.,&Anoop, T.R. (2015). Wave energy resource assessment for the Indian shelf
681 seas. *Renewable energy*, 76, 212-219.<https://doi.org/10.1016/j.renene.2014.11.034>

682 Mackay,E. B. L. (2012). Ocean energy:Resource assessment for wave energy. In A. Sayigh
683 (Eds.), *Comprehensive Renewable Energy* (pp. 11–77).Elsevier.

684 Marshall, A.G., Hemer, M.A., Hendon, H.H.,&McInnes, K.L. (2018). Southern annular mode
685 impacts on global ocean surface waves. *Ocean Modelling*, 129, 58-
686 74.<https://doi.org/10.1016/j.ocemod.2018.07.007>

687 Menéndez, M., Méndez, F.J., Losada, I.J.,& Graham, N.E. (2008). Variability of extreme wave
688 heights in the northeast Pacific Ocean based on buoy measurements. *Geophysical Research*
689 *Letters*, 35(22), L22607.[doi:10.1029/2008GL035394](https://doi.org/10.1029/2008GL035394)

690 Meucci, A., Young, I.R., Aarnes, O.J.,&Breivik, O. (2020). Comparison of wind speed and wave
691 height trends from twentieth century models and satellite altimeters.*Journal of Climate*, 33 (2),
692 611-624.<https://doi.org/10.1175/JCLI-D-19-0540.1>

693 Min, S.K., Cai, W.,&Whetton, P. (2013). Influence of climate variability on seasonal extremes
694 over Australia. *Journal of Geophysical Research: Atmospheres*, 118(2), 643-
695 654.<https://doi.org/10.1002/jgrd.50164>

696 Mollison, D.(1986). Wave climate and the wave power resource. In D.V. Evans & A. F. O. de
697 Falcao (Eds.), *Hydrodynamics of ocean wave-energy utilization* (pp. 133-156).Springer.

698 Mori N, Yasuda T, Mase H, Tom T, Oku Y (2010) Projection of extreme wave climate change
699 under global warming. *Hydrol Res Lett* 4:15–19. <https://doi.org/10.3178/HRL.4.15>

700 Mork, G., Barstow, S., Kabuth, A., & Pontes, M.T. (2010, June). Assessing the global wave
701 energy potential. In *ASME 2010 29th International conference on ocean, offshore and arctic*
702 *engineering* (pp. 447-454). American Society of Mechanical Engineers Digital Collection.

703 Nogaj, M., Parey, S., & Dacunha-Castelle, D. (2007). Non-stationary extreme models and a
704 climatic application. *Nonlinear Processes in Geophysics*, 14(3), 305–316.
705 <https://doi.org/10.5194/npg-14-305-2007>.

706 Patra, A., Min, S.K. and Seong, M.G., 2020. Climate Variability Impacts on Global Extreme
707 Wave Heights: Seasonal Assessment Using Satellite Data and ERA5 Reanalysis. *Journal of*
708 *Geophysical Research: Oceans*, 125(12). <https://doi.org/10.1029/2020JC016754>.

709 Reguero, B.G., Losada, I.J., & Méndez, F.J. (2015). A global wave power resource and its
710 seasonal, interannual and long-term variability. *Applied Energy*, 148, 366-
711 380. <https://doi.org/10.1016/j.apenergy.2015.03.114>

712 Reguero, B.G., Losada, I.J., & Méndez, F.J. (2019). A recent increase in global wave power as a
713 consequence of oceanic warming. *Nature communications*, 10(1), 1-
714 14. <https://doi.org/10.1038/s41467-018-08066-0>

715 Reguero, B.G., Menéndez, M., Méndez, F.J., Mínguez, R., & Losada, I.J. (2012). A Global Ocean
716 Wave (GOW) calibrated reanalysis from 1948 onwards. *Coastal Engineering*, 65, 38-
717 55. <https://doi.org/10.1016/j.coastaleng.2012.03.003>

718 Remya, P.G., Kumar, B.P., Srinivas, G., & Nair, T.M. (2020). Impact of tropical and extra
719 tropical climate variability on Indian Ocean surface waves. *Climate Dynamics*, 54(11-12), 4919-
720 4933. <https://doi.org/10.1007/s00382-020-05262-x>

721 Saji, N.H., Goswami, B.N., Vinayachandran, P.N., & Yamagata, T. (1999). A dipole mode in the tropical
722 Indian Ocean. *Nature*, 401(6751), 360–363. <https://doi.org/10.1038/43854>.

723 Santo, H., Taylor, P.H., Woollings, T., & Poulson, S. (2015). Decadal wave power variability in
724 the North-East Atlantic and North Sea. *Geophysical Research Letters*, 42(12), 4956-
725 4963. doi:10.1002/2015GL064488.

726 Sannasiraj, S.A., & Sundar, V. (2016). Assessment of wave energy potential and its harvesting
727 approach along the Indian coast. *Renewable energy*, 99, 398-
728 409. <https://doi.org/10.1016/j.renene.2016.07.017>

729 Semedo, A., Sušelj, K., Rutgersson, A., & Sterl, A. (2011). A global view on the wind sea and
730 swell climate and variability from ERA-40. *Journal of Climate*, 24(5), 1461-
731 1479. <https://doi.org/10.1175/2010JCLI3718.1>

732 Shanab, P. R., & Kumar, V. S. (2014). Trends in surface wind speed and significant wave height
733 as revealed by ERA-Interim wind wave hindcast in the Central Bay of Bengal. *International*
734 *Journal of Climatology*, 35(9), 2654–2663. doi: 10.1002/joc.4164

735 Sterl, A., & Caires, S. (2005). Climatology, variability and extrema of ocean waves: The
736 Web-based KNMI/ERA-40 wave atlas. *International Journal of Climatology: A Journal of the*
737 *Royal Meteorological Society*, 25(7), 963-977. doi: 10.1002/joc.1175

738 Stevenson, S. L. (2012). Significant changes to ENSO strength and impacts in the twenty-first
739 century: Results from CMIP5. *Geophysical Research Letters*, 39, L17703.
740 <https://doi.org/10.1029/2012GL052759>

741 Stopa, J. E., Cheung, K. F., Tolman, H. L., & Chawla, A. (2013). Patterns and cycles in the Climate
742 Forecast System Reanalysis wind and wave data. *Ocean Modelling*, 70, 207–220.
743 <https://doi.org/10.1016/j.ocemod.2012.10.005>.

744 Stuecker, M.F., Timmermann, A., Jin, F.F., Chikamoto, Y., Zhang, W., Wittenberg, A.T., et
745 al.(2017). Revisiting ENSO/Indian Ocean dipole phase relationships. *Geophysical Research*
746 *Letters*, 44(5), 2481-2492.

747 Wandres, M., Pattiaratchi, C., Hetzel, Y.,&Wijeratne, E.M.S. (2018). The response of the
748 southwest Western Australian wave climate to Indian Ocean climate variability. *Climate*
749 *dynamics*, 50(5-6), 1533-1557.

750 Wang, X. L., &Swail, V. R.(2001). Changes of extreme wave heights in northern hemisphere
751 oceans and related atmospheric circulation regimes.*Journal of climate*,14, 2204-2221.

752 Wang, X. L., &Swai, V. R.(2006). Historical and possible future changes of wave heights in
753 northern hemisphere ocean InW. Perrie (Eds.),*Atmosphere Ocean Interactions*(pp. 240) Wessex
754 Institute of Technology Press, Southampton, U.K.

755 Wang, X. L., Feng, Y.,&Swail, V. R.(2012). North Atlantic wave height trends as reconstructed
756 from the 20th century reanalysis, *Geophysical Research Letters*, 39,
757 L18705.doi:10.1029/2012GL053381.

758 Wang, X. L., Swail, V. R.,Zwiers, F. W., Zhang, X.,& Feng, Y.(2009). Detection of external
759 influence on trends of atmospheric storminess and ocean wave height.*Climate Dynamics*,32,
760 189-203.doi:10.1007/s00382-008-0442-2.

761 Webster, P. J., Moore, A. M., Loschnigg, J. P., &Leben, R. R. (1999).Coupled ocean-atmosphere
762 dynamics in the Indian Ocean during 1997–98. *Nature*, 401(6751), 356–360.
763 <https://doi.org/10.1038/43848>.

764 Yang, S.,& Oh, J. (2020).Effects of modes of climate variability on wave power during boreal
765 summer in the western North Pacific. *Scientific reports*, 10(1),1-10.

766 Yang, S., & Oh, J. (2018). Long-Term Changes in the Extreme Significant Wave Heights on the
767 Western North Pacific: Impacts of Tropical Cyclone Activity and ENSO. *Asia-Pacific Journal of*
768 *Atmospheric Sciences*, 54(1), 103-109.

769 Young, I. R. (1999) Seasonal variability of the global ocean wind and wave climate.
770 *International Journal of Climatology*, 19(9), 931–950.

771 Young, I. R., Zieger, S., & Babanin, A. V. (2011): Global trends in wind speed and wave
772 height. *Science*, 332, 451-455. doi:10.1126/science.1197219.

773 Young, I. R., Vinoth, J., Zieger, S., & Babanin, A. V. (2012). Investigation of trends in
774 extreme value wave height and wind speed, *Journal of Geophysical Research*. 117,
775 C00J06. doi:10.1029/2011JC007753.

776 Young, I.R., & Ribal, A. (2019). Multiplatform evaluation of global trends in wind speed and
777 wave height. *Science*, 364(6440), 548-552.

778 Yuan, Y., Zhou, W., Chan, J. C. L., & Li, C. (2008). Impacts of the basin-wide Indian Ocean
779 SSTA on the South China Sea summer monsoon onset. *International Journal of Climatology: A*
780 *Journal of the Royal Meteorological Society*, 28(12), 1579–1587.
781 <https://doi.org/10.1002/joc.1671>.

782 Zhang, J., Wang, W., & Guan, C. (2011). Analysis of the global swell distributions using
783 ECMWF Re-analyses wind wave data. *Journal of Ocean University of China*, 10(4), 325-330.

784 Zhang, X.B., Wang, J.F., Zwiers, F.W., & Groisman, P.Y. (2010). The influence of large-scale climate vari-
785 ability on winter maximum daily precipitation over North America. *Journal of Climate*, 23(11),
786 2902–2915. <https://doi.org/10.1175/2010JCLI3249.1>.

787 Zhang, Y., Wallace, J. M., & Battisti, D. S. (1997) ENSO-like interdecadal variability: 1900–93.
788 *Journal of Climate*, 10, 1004–1020. doi:10.1175/1520-0442(1997)010<1004:ELIV.2.0.CO;2.

789 Zheng, K., Sun, J., Guan, C., & Shao, W. (2016). Analysis of the global swell and wind sea
790 energy distribution using WAVEWATCH III. *Advances in*
791 *Meteorology*. <https://doi.org/10.1155/2016/8419580>

792

793 **Table1.** A list of previous studies on natural climate variability influence on WP in comparison
794 with the current study

Reference	Data (Period)	(Season)Variables	Climate Variability	Analysis Domain	Analysis Method
Bromirski et al. (2013)	WW3 wave model (1948-2008)	(winter and summer) 90 th percentile SWH, PWP, WP	PDO, ENSO, PNA	North Pacific	Linear trend and EOF
Bromirski and Cayan (2015)	WW3 wave model (1948-2008)	(winter and summer) 90 th percentile SWH, PWP, WP	NAO, PNA, PDO, ENSO	North Atlantic	Linear trend and EOF
Reguero et al. (2015)	WW3 wave model (1948-2008)	(Annual) mean SWH, MWP, WP	AO, AMO, EA, NAO, SOI, TNA, PNA, WP, EP-NP, SAM, SCA, DMI	Global	Correlation analysis
Reguero et al. (2019).	WW3 wave model (1948-2008), satellite altimetry (1992–2008)	(Annual) mean SWH, MWP, WP	ENSO and AMO	Global	Linear trend
Yang & Oh (2020)	WW3 wave model (1979-2009)	(summer) 99 th percentile SWH, PWP, WP	ENSO, PDO	western NP	Regression analysis, Composite analysis (ENSO and PDO)
Recent study	ERA5 (1979-2019)	(seasonal) mean and extreme SWH, PWP, WP	ENSO, IOD, PDO	Indo-Pacific	Non-stationary GEV, Composite analysis (ENSO with IOD and PDO)

795

796

797 **Table 2:** Correlation coefficients between the seasonal N34 with DMI and PDO indices for the
 798 period 1979–2019. All indices are linearly detrended. Statistically significant correlations at the
 799 5% and 1% significance levels are marked with * and **, respectively.

	N34– DMI	N34 – PDO
DJF	0.071	0.397**
MAM	-0.125	0.458**
JJA	0.312*	0.437**
SOA	0.620**	0.545**

800

801

802 **Table 3:** List of years when a combination of El Niño or La Niña and/or positive or negative
 803 IOD events greater than plus or minus one-half standard deviation occurred during the period
 804 1979–2019 for (a) JJA, and (b) SON.

(a) JJA	ENSO(+) or El Niño	ENSO(–) or La Niña
DMI(+) or pIOD	1982, 1983, 1991, 1993, 1994, 1997, 2012, 2015, 2019	1999, 2007, 2008
DMI(–) or nIOD	1990, 1992, 2002, 2004, 2009	1981, 1984, 1989, 1995, 1996, 1998, 2010, 2013, 2016
(b) SON	ENSO(+) or El Niño	ENSO(–) or La Niña
DMI(+) or pIOD	1982, 1986, 1987, 1991, 1994, 1997, 2002, 2006, 2015, 2018, 2019	1983, 1985, 2011
DMI(–) or nIOD	1979, 2003, 2009, 2014	1981, 1984, 1988, 1989, 1995, 1996, 1998, 1999, 2001, 2005, 2010, 2016

805

806

807

808

809 **Table 4:** List of years when a combination of El Niño or La Niña and/or positive or negative
810 PDO events greater than plus or minus one-half standard deviation occurred during the period
811 1979–2019 for (a) DJF, (b) MAM, (c) JJA, and (d) SON.

812

(a) DJF	ENSO(+) or El Niño	ENSO(-) or La Niña
PDO(+) or pPDO	1986, 1987, 1997, 2002, 2009, 2014, 2015, 2018	1983, 1984, 1985, 2005, 2017
PDO(-) or nPDO	1990, 1994	1988, 1998, 1999, 2007, 2008, 2010, 2011, 2012
(b) MAM	ENSO(+) or El Niño	ENSO(-) or La Niña
PDO(+) or pPDO	1983, 1987, 1992, 1993, 1994, 1995, 1997, 1998, 2005, 2015, 2016, 2017, 2019	1981, 1984, 1986, 1988, 1996
PDO(-) or nPDO	1982, 1991, 2002	1985, 1989, 1999, 2000, 2001, 2007, 2008, 2009, 2011, 2012, 2013
(c) JJA	ENSO(+) or El Niño	ENSO(-) or La Niña
PDO(+) or pPDO	1983, 1987, 1992, 1993, 1997, 2015, 2019	1995, 2007, 2016
PDO(-) or nPDO	1982, 1991, 1994, 2002, 2009, 2012	1984, 1998, 1999, 2000, 2008, 2010, 2013
(d) SON	ENSO(+) or El Niño	ENSO(-) or La Niña
PDO(+) or pPDO	1979, 1986, 1987, 1991, 1997, 2002, 2003, 2009, 2014, 2015, 2018, 2019	1983, 1984, 1995, 2016, 2017
PDO(-) or nPDO	1994, 2006	1985, 1988, 1989, 1998, 1999, 2000, 2001, 2005, 2007, 2008, 2010, 2011

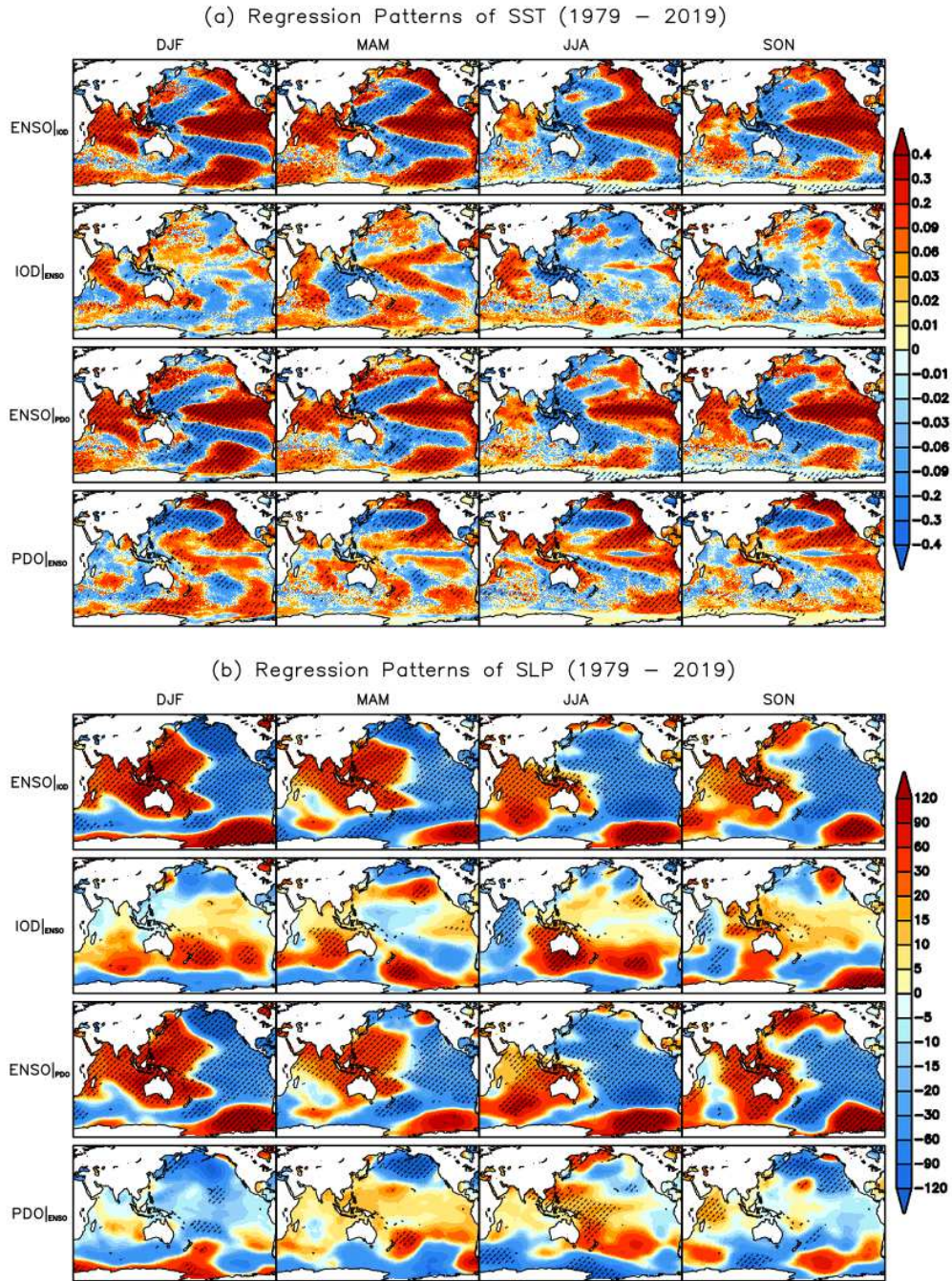
813

814

815

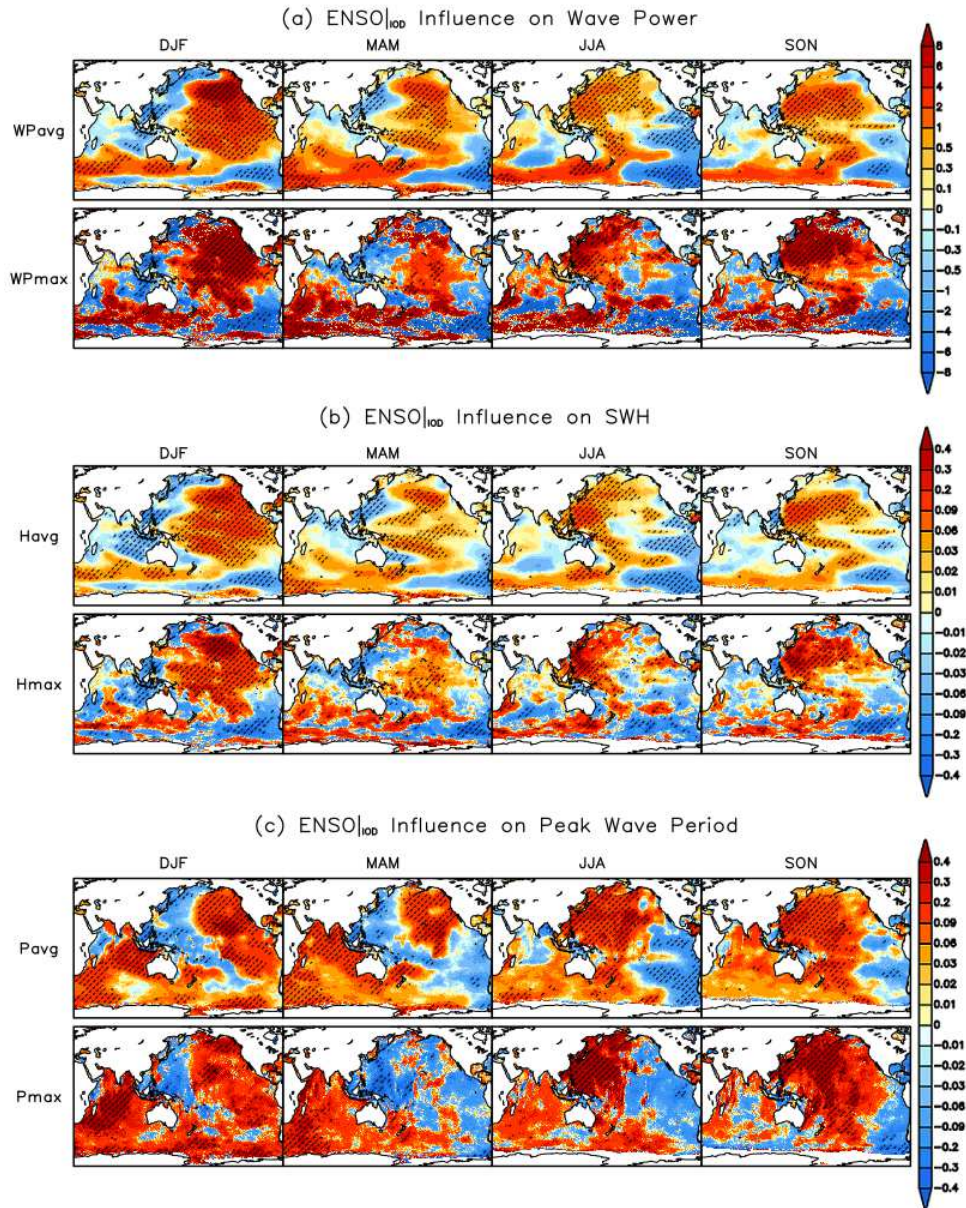
816

817



818

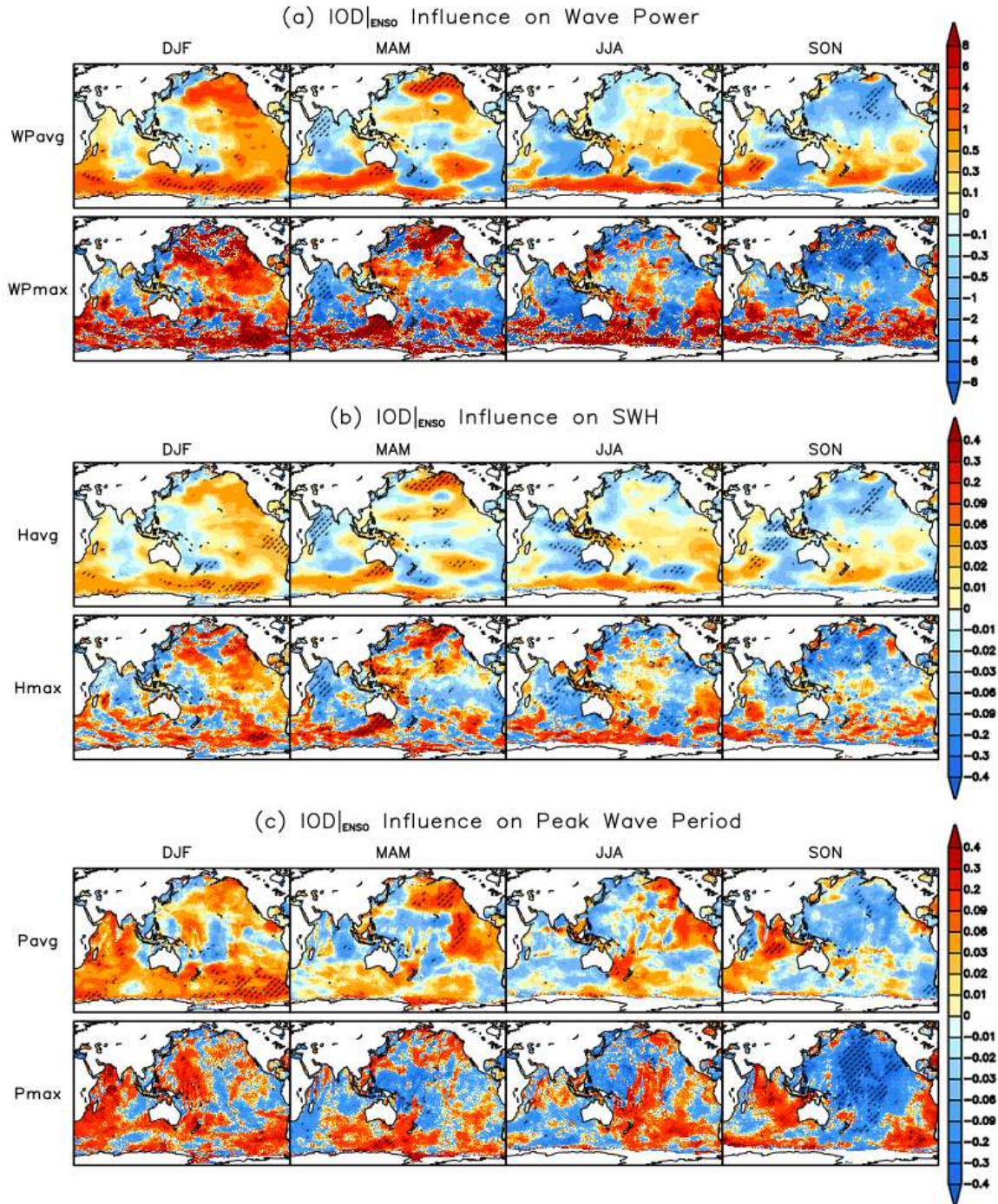
819 **Figure 1.** Seasonal regression patterns of mean (a) SST (in K) and (b) SLP (in Pa) onto
 820 ENSO_{IOD}, IOD_{ENSO}, ENSO_{PDO}, and PDO_{ENSO} in the Indo–Pacific Ocean over the period 1979–
 821 2019. Hatching represents the statistically significant regions at the 5% level.



822

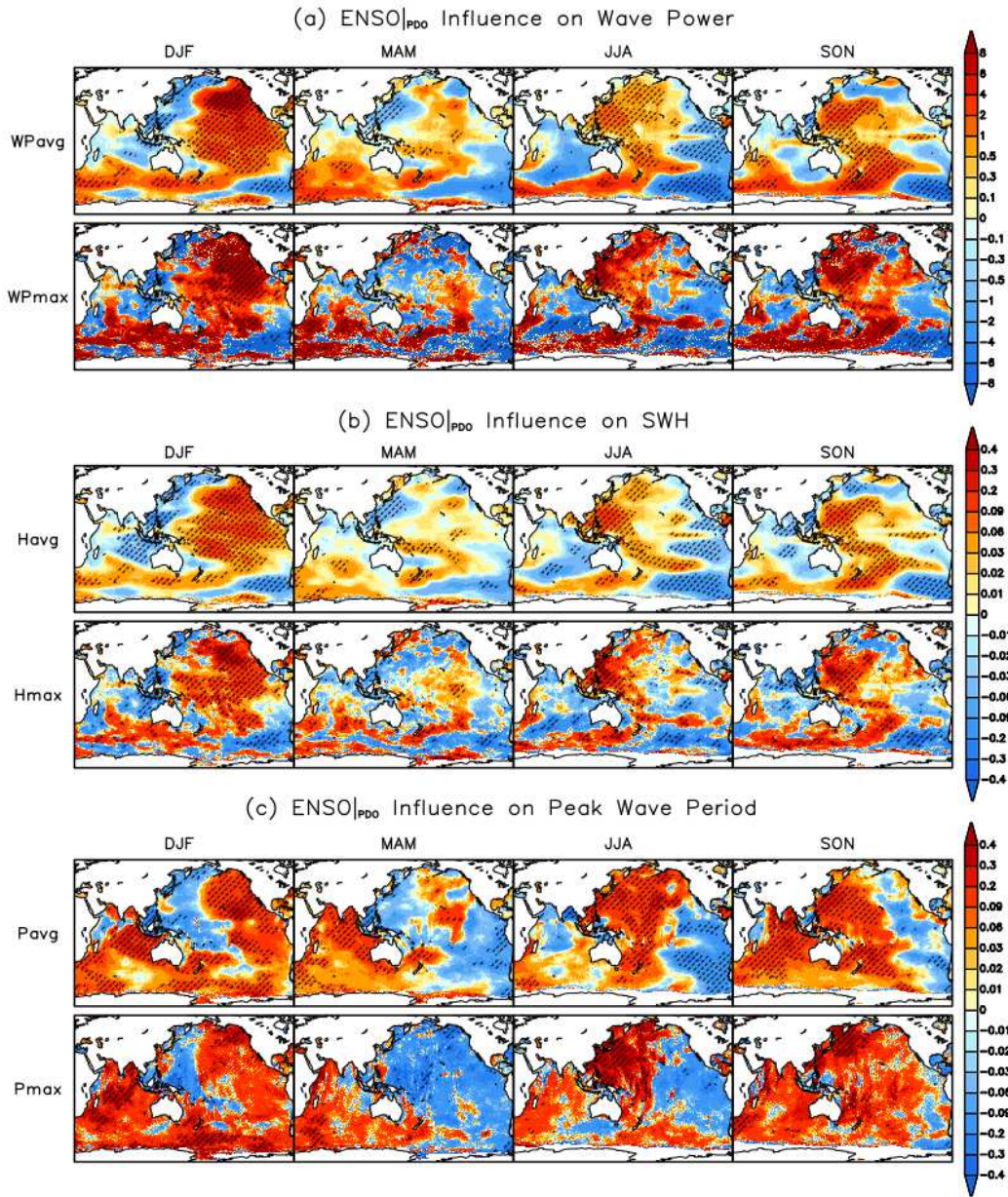
823 **Figure 2.** The seasonal ENSO influence independent of IOD (denoted as $ENSO|_{IOD}$), obtained
 824 after the removal of IOD signals, on the mean and extreme WP (i.e., WPavg and WPmax), SWH
 825 (Havg and Hmax) and PWP (Pavg and Pmax) in the Indo–Pacific Ocean over the period 1979–
 826 2019. Hatching represents statistically significant regions at the 5% level. The unit of WP, SWH
 827 and PWP are given as kilowatts per meter (kW/m), meter (m) and seconds (s).

828



829

830 **Figure 3.** As in Fig. 2, but for the seasonal IOD influence independent of ENSO (denoted as
 831 $IOD|_{\text{ENSO}}$), obtained after the removal of ENSO signals.

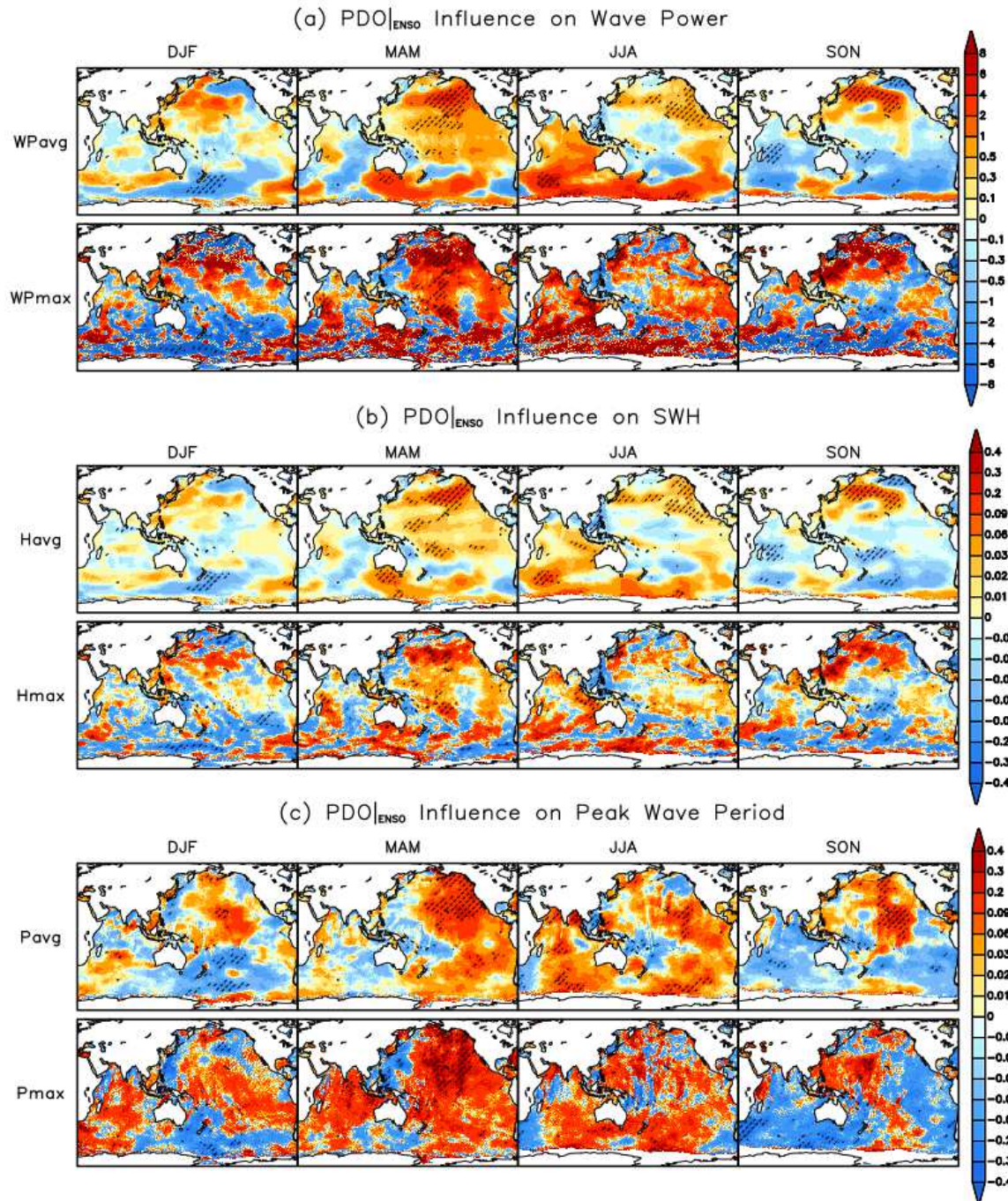


832

833 **Figure 4.** As in Fig. 2, but for the seasonal ENSO influence independent of PDO (denoted as

834 ENSO_{|PDO}), obtained after the removal of PDO signals.

835

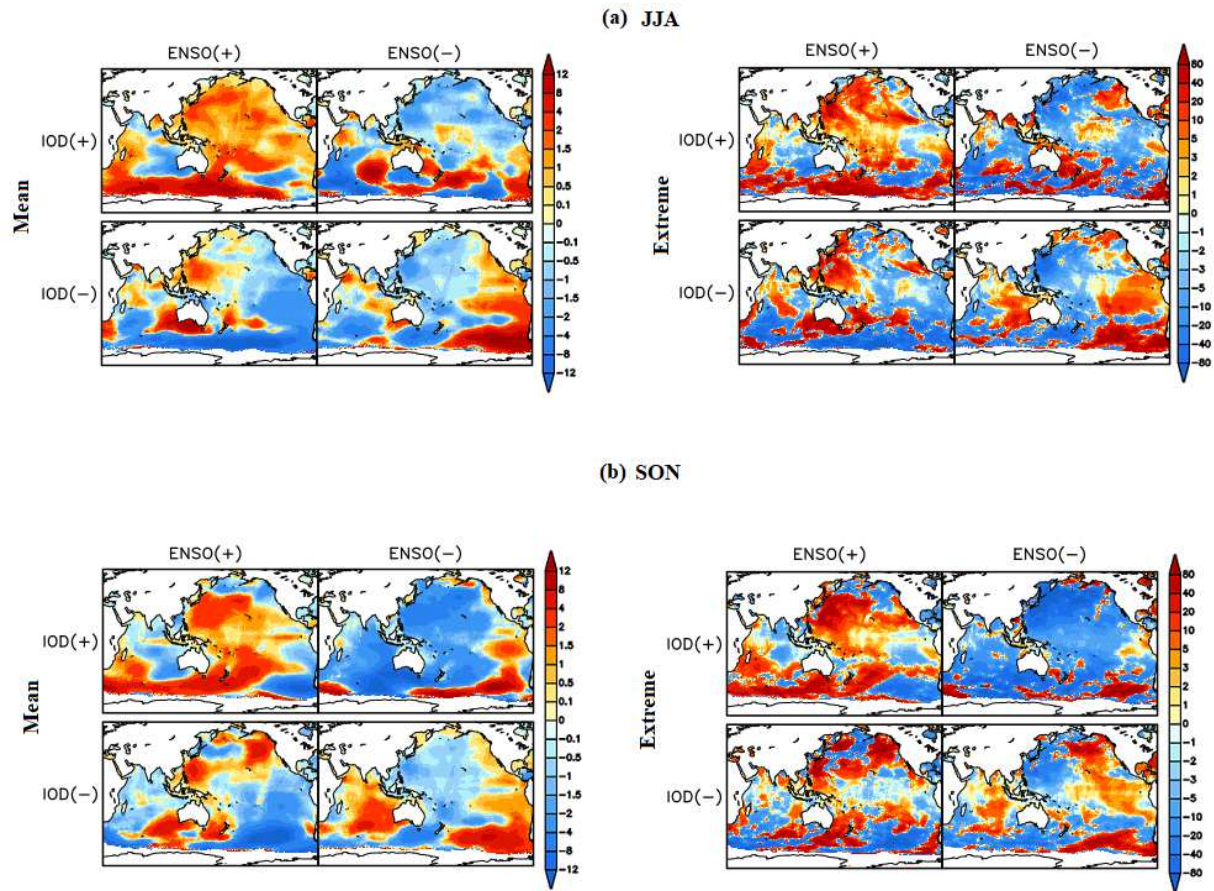


836

837 **Figure 5.** As in Fig. 2, but for the seasonal PDO influence independent of ENSO (denoted as
 838 $\text{PDO}|_{\text{ENSO}}$), obtained after the removal of ENSO signals.

839

840



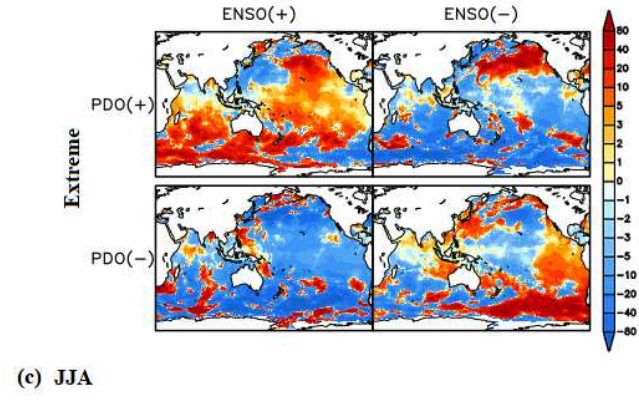
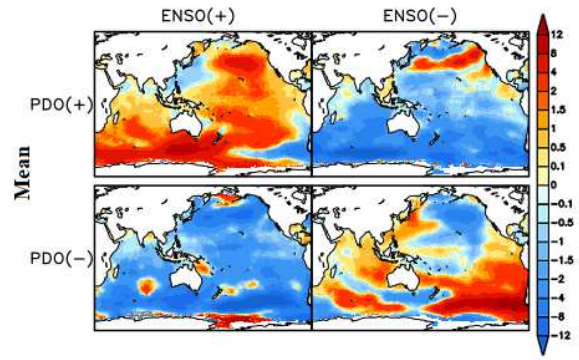
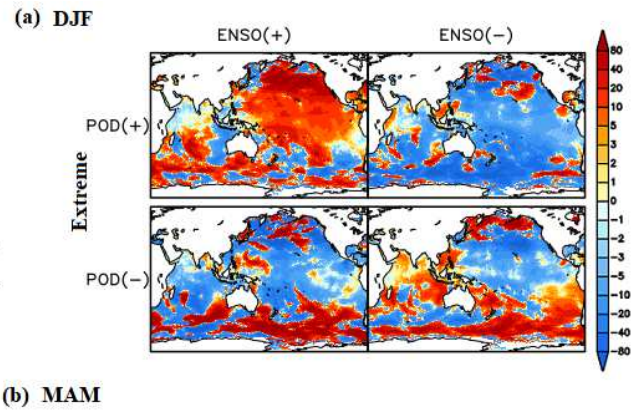
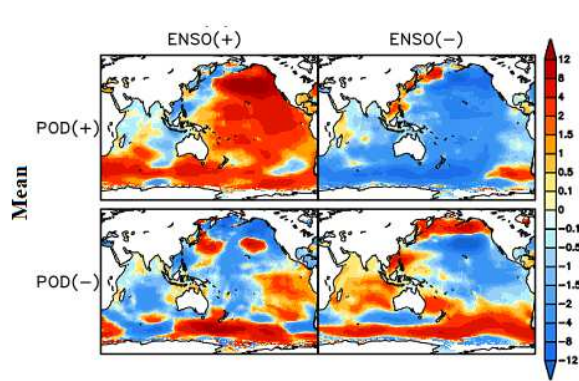
841

842 **Fig. 6.** Composite patterns of mean WP (left panels) and extreme WP anomalies (right panels)

843 during (a) JJA and (b) SON for the four different combinations of ENSO and IOD: El

844 Niño/pIOD, La Niña/pIOD, El Niño/nIOD, and La Niña/nIOD over the 41 year period from

845 1979–2019 (see list of years in Table 3).



847 **Fig. 7.** Composite patterns of mean WP (left panel) and extreme WP anomalies (right pannel)
848 during (a) DJF, (b) MAM, (c) JJA, and (d) SON for the four different combinations of ENSO
849 and PDO: El Niño/pPDO, La Niña/pPDO, El Niño/nPDO, and La Niña/nPDO over the 41 year
850 period from 1979–2019 (see list of years in Table 4).

851

852

853

854

855

856

857

858

859

860

861

862

863

864

865

866

867

868

869

Figures

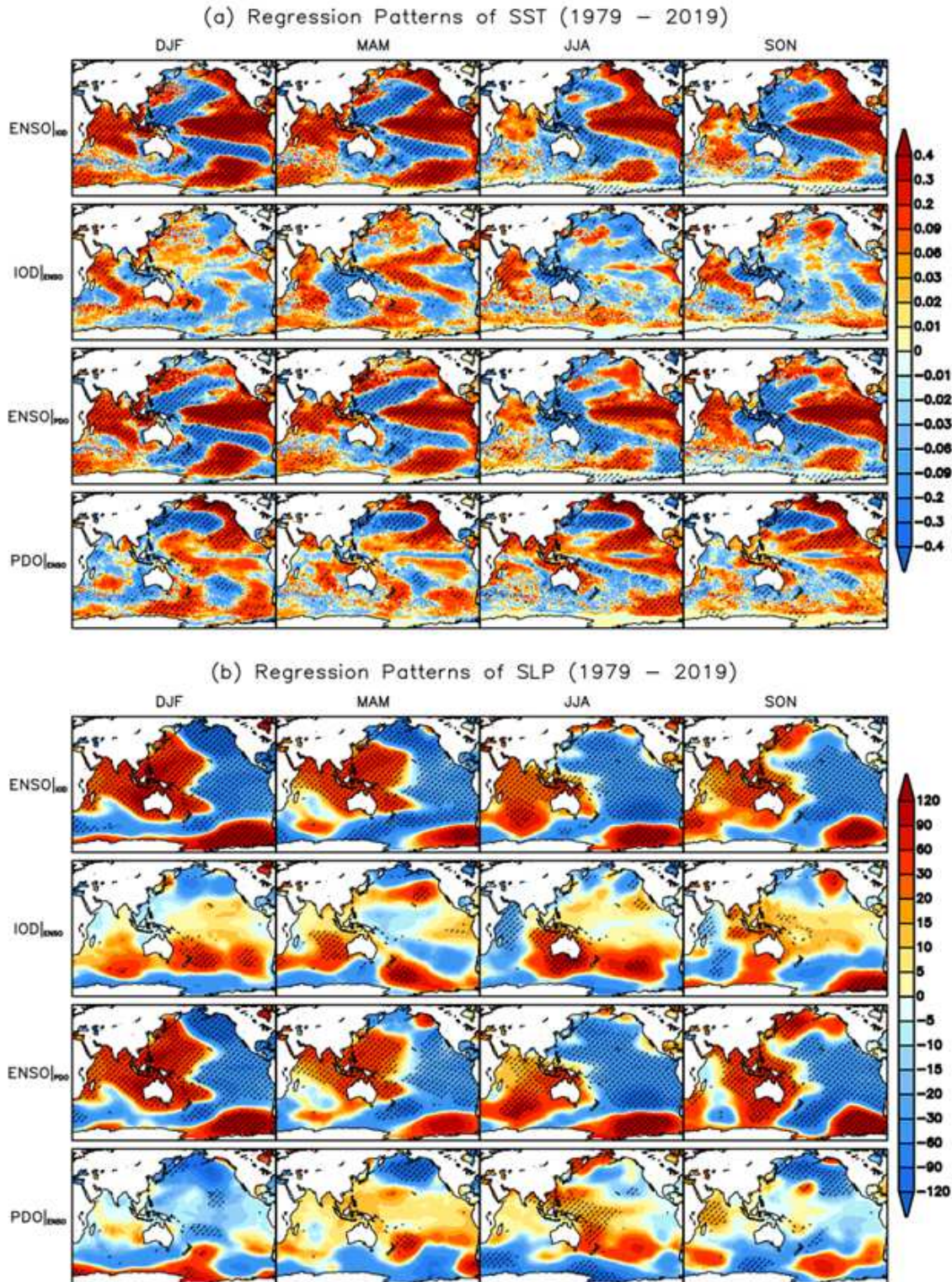


Figure 1

Seasonal regression patterns of mean (a) SST (in K) and (b) SLP (in Pa) onto ENSO|IOD, IOD|ENSO, ENSO|PDO, and PDO|ENSO in the Indo–Pacific Ocean over the period 1979–2019. Hatching represents the statistically significant regions at the 5% level. Note: The designations employed and the presentation

of the material on this map do not imply the expression of any opinion whatsoever on the part of Research Square concerning the legal status of any country, territory, city or area or of its authorities, or concerning the delimitation of its frontiers or boundaries. This map has been provided by the authors.

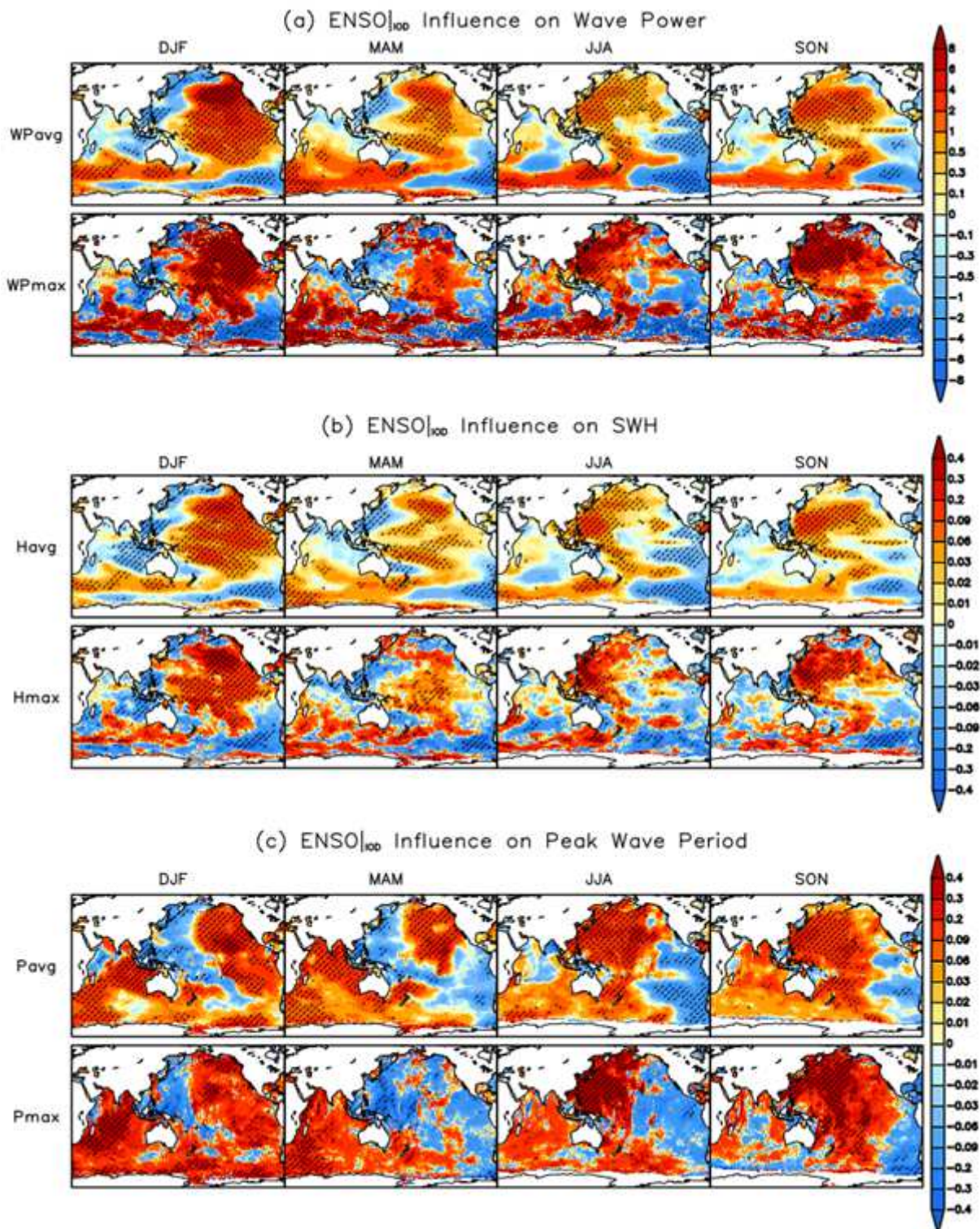


Figure 2

The seasonal ENSO influence independent of IOD (denoted as ENSO_{|IOD}), obtained after the removal of IOD signals, on the mean and extreme WP (i.e., WPavg and WPmax), SWH (Havg and Hmax) and PWP

(Pavg and Pmax) in the Indo–Pacific Ocean over the period 1979–2019. Hatching represents statistically significant regions at the 5% level. The unit of WP, SWH and PWP are given as kilowatts per meter (kW/m), meter (m) and seconds (s). Note: The designations employed and the presentation of the material on this map do not imply the expression of any opinion whatsoever on the part of Research Square concerning the legal status of any country, territory, city or area or of its authorities, or concerning the delimitation of its frontiers or boundaries. This map has been provided by the authors.

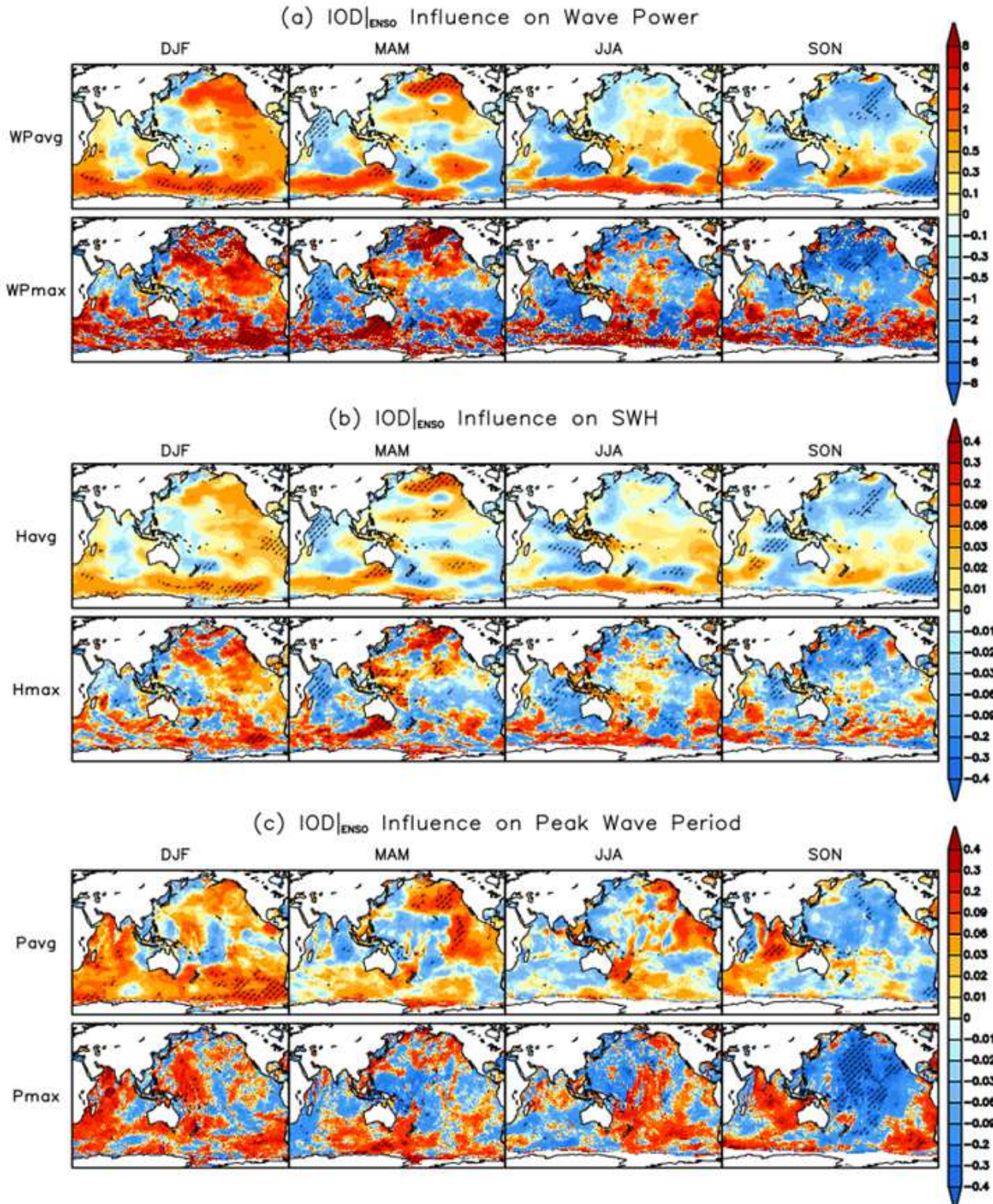


Figure 3

As in Fig. 2, but for the seasonal IOD influence independent of ENSO (denoted as IOD|ENSO), obtained after the removal of ENSO signals. Note: The designations employed and the presentation of the material on this map do not imply the expression of any opinion whatsoever on the part of Research Square concerning the legal status of any country, territory, city or area or of its authorities, or concerning the delimitation of its frontiers or boundaries. This map has been provided by the authors.

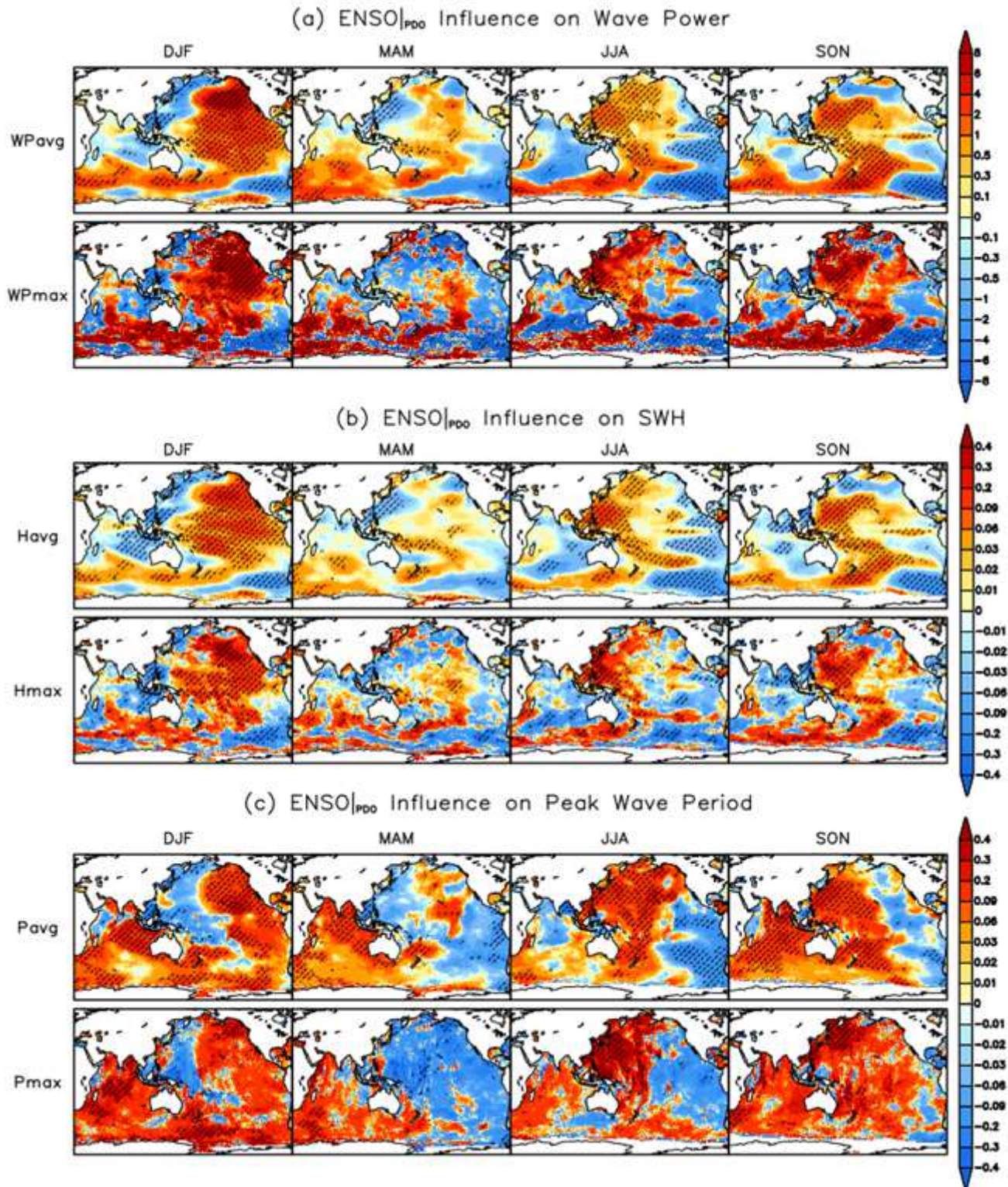


Figure 4

As in Fig. 2, but for the seasonal ENSO influence independent of PDO (denoted as ENSO|PDO), obtained after the removal of PDO signals. Note: The designations employed and the presentation of the material on this map do not imply the expression of any opinion whatsoever on the part of Research Square concerning the legal status of any country, territory, city or area or of its authorities, or concerning the delimitation of its frontiers or boundaries. This map has been provided by the authors.

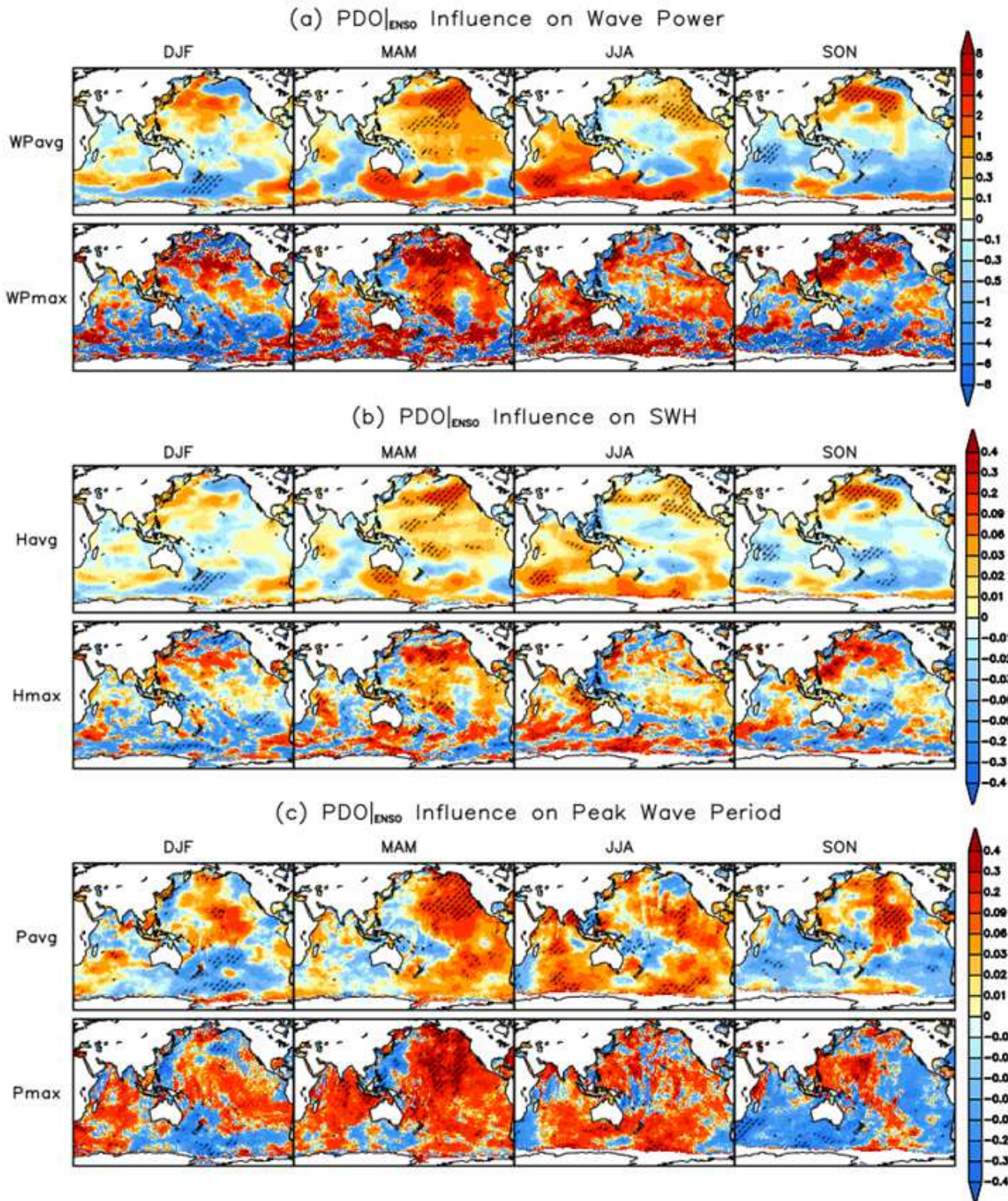


Figure 5

As in Fig. 2, but for the seasonal PDO influence independent of ENSO (denoted as PDO|ENSO), obtained after the removal of ENSO signals. Note: The designations employed and the presentation of the material on this map do not imply the expression of any opinion whatsoever on the part of Research Square concerning the legal status of any country, territory, city or area or of its authorities, or concerning the delimitation of its frontiers or boundaries. This map has been provided by the authors.

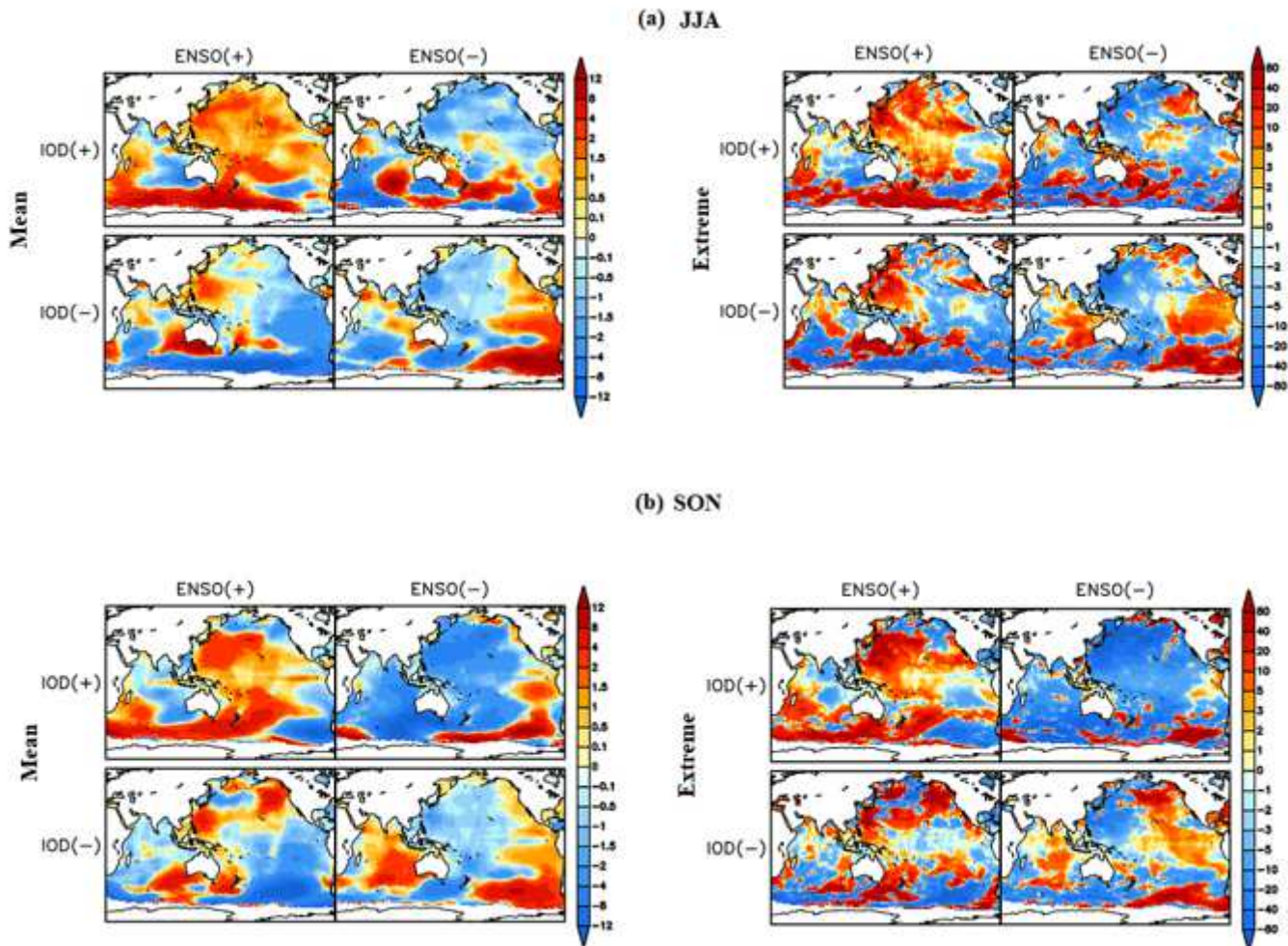


Figure 6

Composite patterns of mean WP (left panels) and extreme WP anomalies (right panels) during (a) JJA and (b) SON for the four different combinations of ENSO and IOD: El Niño/pIOD, La Niña/pIOD, El Niño/nIOD, and La Niña/nIOD over the 41 year period from 1979–2019 (see list of years in Table 3). Note: The designations employed and the presentation of the material on this map do not imply the expression of any opinion whatsoever on the part of Research Square concerning the legal status of any country, territory, city or area or of its authorities, or concerning the delimitation of its frontiers or boundaries. This map has been provided by the authors.

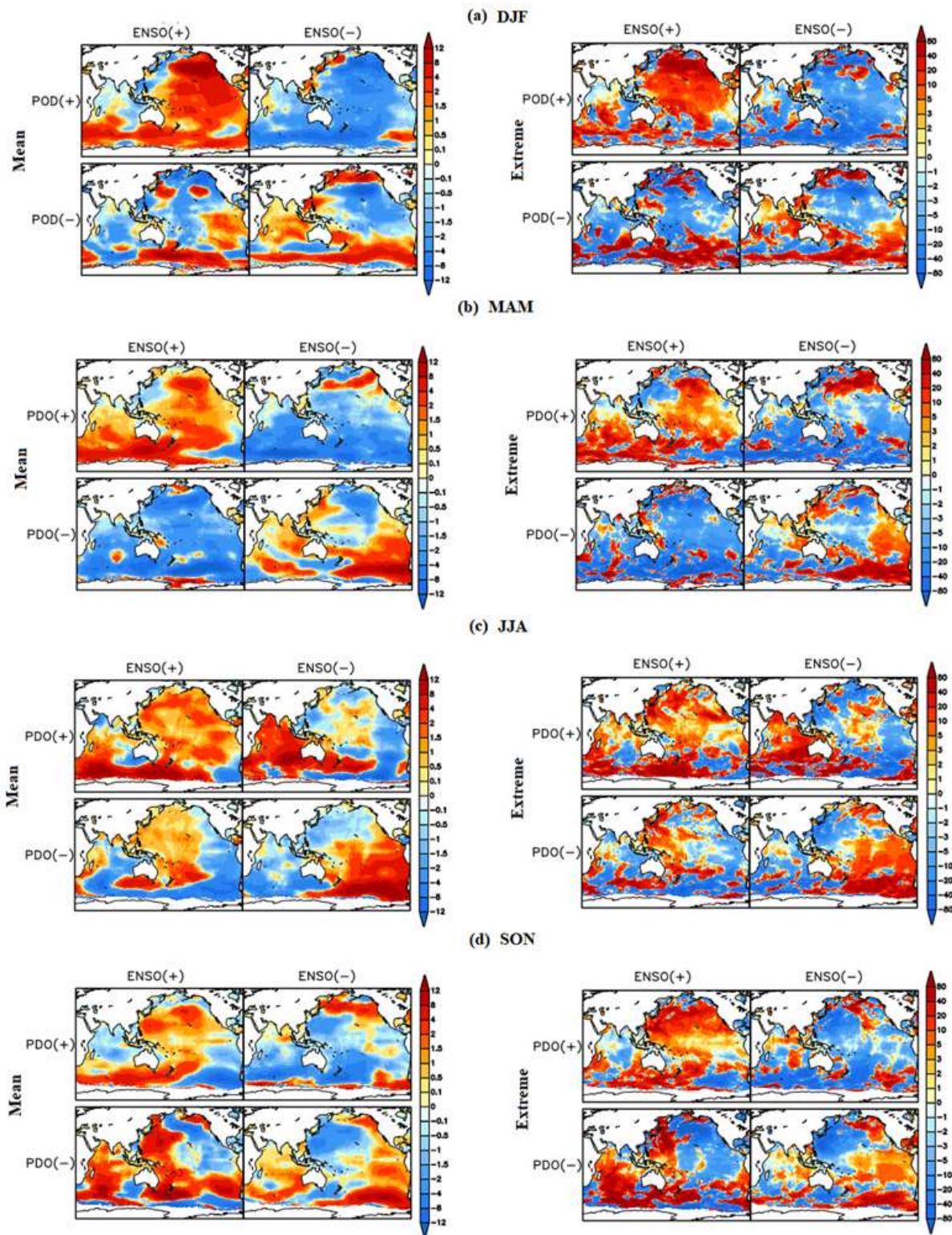


Figure 7

Composite patterns of mean WP (left panel) and extreme WP anomalies (right panel) during (a) DJF, (b) MAM, (c) JJA, and (d) SON for the four different combinations of ENSO and PDO: El Niño/pPDO, La Niña/pPDO, El Niño/nPDO, and La Niña/nPDO over the 41 year period from 1979–2019 (see list of years in Table 4). Note: The designations employed and the presentation of the material on this map do not imply the expression of any opinion whatsoever on the part of Research Square concerning the legal

status of any country, territory, city or area or of its authorities, or concerning the delimitation of its frontiers or boundaries. This map has been provided by the authors.

Supplementary Files

This is a list of supplementary files associated with this preprint. Click to download.

- [Supplimentaryfigures.docx](#)